Study of two-kaon correlations in central Pb + Pb collisions at 158 A GeV/c

DISSERTATION

Takeshi Kohama

Department of Physical Science,
Graduate School of Science,
Hiroshima University

Kagamiyama 1-3-1, Higashi-Hiroshima, 739-8526, Japan

January, 2002

Abstract

The "Quark–gluon plasma" (QGP) phase is a new state of matter, which might be appeared around 10 μs after the Big–bang. However, the QGP phase has not been experimentally identified yet. To recreate such a new state of matter in a laboratory, experiments of ultra–relativistic heavy–ion collisions are considered. As one of these experiments, we measure 158 GeV/c Pb + Pb collisions from the Super–Proton–Synchrotron (SPS) at CERN. A method of kaon interferometry are used to investigate a source of secondary particles from the Pb + Pb collisions.

The NA44 focusing spectrometer is used for the measurements of momentum and identification of each particles. Datasets in two different transverse momentum region ($< p_T > = 0.25$ and 0.91 GeV/c) are taken at the mid–rapidity for the central collisions.

Two–kaon correlation functions are parametrized with the three–dimensional Gaussian source for the lower p_T data, while the two–dimensional Gaussian source are used to parameterize the correlation function of the higher p_T data.

The results are compared with the kaon interferometry measurements in p + Pb and S + Pb. The source parameters increase with the projectile nuclear radius increase and larger than that in any case. The pion source size parameters are much larger than the kaon source size, which suggests that the system expands before the freeze–out. The kaon source parameters decrease with increasing transverse momentum and are scaled to the transverse momentum with the pion source size parameters. This suggests an expanding source. According to a simple hydro-dynamical model, the freeze–out time is deduced to be 7–10 fm/c assuming a homogeneous freeze–out temperature 100–140 MeV.

We derived the duration time of kaon emission, and $\Delta\tau = 2.2 \pm 5.2(\text{stat.}) \pm 6.1(\text{syst.})$ The kaon duration time is short and similar to those observed for pions in the same colliding system and for kaons in the S + Pb collisions. The present result excludes simple scenarios of a prolonged mixed phase anticipated in a first–order phase transition from a QGP phase.

Contents

Chapter 1

Introduction

Interest to the universe is an intrinsic property of people, not only philosophers in history. Matter in the early universe just after the big–bang is expected to be in a new state, quark–gluon plasma. Studying the quark–gluon plasma reveals a feature of the early universe.

In this thesis, size and dynamics of particle source in ultra–relativistic heavy ion collisions are discussed, which is very hot and dense, and where the quark–gluon plasma can be created. To do that, I analyze the data taken by data of lead–on–lead collisions at 158 A GeV. Particle interferometry (aka the HBT method) are used as a method of data analysis.

In the chapter 1, quark–gluon plasma, ultra–relativistic heavy ion collisions and particle interferometry are briefly introduced. After that, I explain what is motivation in this study and why this method is useful. The experimental apparatus (i.e. the NA44 spectrometer) and a procedure of the data analysis are explained in the chapter 2 and the chapter 3, respectively. The source size of particles emitted in lead–on-lead collisions are shown in the chapter 4. Using the results of the source size, several discussions are made in the chapter 5. There is conclusion of this thesis in the chapter 6.

In this thesis, the natural unit system (c and $\hbar$ is defined as 1) is some-

times used. So that a unit of mass and momentum may be indicated by "MeV" or "GeV". Moreover, the unit of energy ("MeV") is used as a unit of temperature, defining the Boltzmann constant k_B as 1, too. The "A GeV" means a unit of beam energy of heavy–ion per nucleon, since A indicates a mass number (i.e. the number of nucleons in the heavy–ion).

1.1 Quark–gluon plasma

1.1.1 QCD and deconfinement

In early 1960s, Gell-Mann and Zweig explained the hadronic structure by the quark model. In this model, mesons are to be described as quark–antiquark bound states, and baryons as three–quark bound states. Any isolated single quarks have never been observed experimentally. This feature of quark are knows as "confinement" of quarks into the hadrons, which is phenomenologically explained by the potential of the strong interaction:

$$V(r) = -\frac{4}{3}\frac{\alpha_s(r)\ \hbar c}{r} + kr$$

In short distance, strength of the interaction relates to $1/r$, and quarks (and gluons) behave in the asymptotic freedom from the strong interaction. When $k = 1$ GeV/fm and $\alpha_s = 0.25$, the mass of mesons can be explained well. Gluons have the same feature as quarks.

On the other hand, the study of the quark model was progressed using with the gauge theory, and established as the quantum chromodynamics (QCD). The predictions of QCD calculated by many theorists are consistent with results of many experiments. Therefore most of physicists give recognition to QCD.

We can expect disappearing of confinement (deconfinement) from hadrons in extreme hot and dense situation. A deconfinement state of the material

is called as quark–gluon plasma, which is an analogy to the QCD from usual plasma in the material physics field. The bag model by the MIT group intuitively explains the deconfinement. Study of the lattice QCD which can calculate in the non-perturbative region numerically, finds deconfinement of quark and gluon within hotter hadrons than a critical temperature $T_c \sim 140$ – 200 MeV.

In the quark–gluon plasma, the potential $V(r)$ between two quarks decreases by the Debye screening as:

$$V(r) = -\frac{4}{3}\frac{\alpha_s(r)\ \hbar c}{r}\exp\left(-r/r_D\right) + kr\frac{1-\exp\left(-r/r_D\right)}{r/r_D},$$

where r_D is the Debye radius of the strong interaction. Since quarks in the quark–gluon plasma interact circumambient quarks, average strong field to a quark is expected to be little. Quarks in the quark–gluon plasma can be moved in free.

1.1.2 Phase diagram of quark matter

We have introduced the quark–gluon plasma so far. Quarks and gluons are deconfined in hot and dense situation. This can be drawn a figure of a phase diagram,[1] with a transition from a hadronic gas (HG) at low energy densities to a quark–gluon plasma at high energy densities. The critical energy density ϵ_c is of the order of 1 GeV/fm^3.It can be reached by either heating matter at zero net baryon density to a temperature of about $T_c \sim$ 140 – 200 MeV or by compressing cold nuclear matter to baryon density about $\rho_c \sim 5$ – 20 ρ_0 (ρ_0 is a density of nuclear), where nucleon distribution is overlapped with the neighbor nucleons.

The figure 1.2 shows a phase diagram. The vertical axis shows temperature T and the horizontal axis shows the baryon chemical potential μ

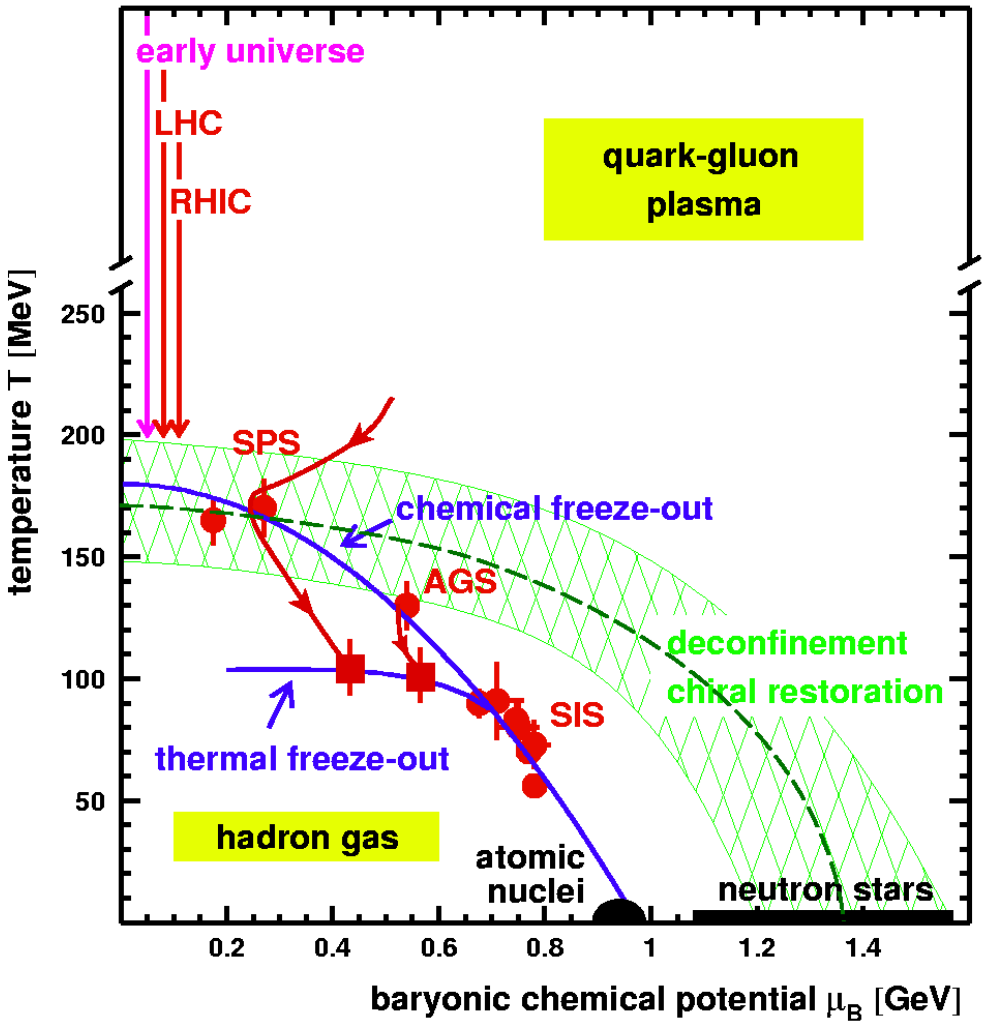

Figure 1.1: The sketch of the QCD phase diagram, superimposing plots of temperature T vs. baryon chemical potential μ_B[1]. The μ_B is associated with the net baryon density ρ_B. See text for a more description and discussion about this plot.

associated with net baryon density. The dashed line shows the expected phase transition, and the cross–hatched region indicates its present theoretical uncertainty.

The quark–matter is expected to exist in a state of the quark–gluon plasma at the early universe (where it is extremely hot) or center region of neutron stars (where it may be enough dense for the transition). Since we think ultra–relativistic heavy ion collisions by huge accelerators (SPS, RHIC and LHC) are an only way to create the quark–gluon plasma with human art. That is introduced in the next section,

1.2 Ultra–relativistic heavy ion collisions

Ultra–relativistic heavy ion collisions provide us an opportunity to study extreme hot and dense nuclear matter in a laboratory. They have possibility to create the quark–gluon plasma. Many experiment groups investigate to reveal a feature of heavy ion collisions. Their ultimate goal is to confirm an existence of the quark–gluon plasma, and to study its properties.

From 1980's, two heavy–ion accelerators supply ultra–relativistic heavy ion collisions; the alternative gradient synchrotron (AGS) at the Brookhaven national laboratory (BNL) and the super proton synchrotron (SPS)[1] at the European organization for nuclear research (CERN). Experiments for gold–on–gold collisions with higher energy (100 A GeV + 100 A GeV) used the relativistic heavy ion collider (RHIC) at BNL have also started its experiments since summer of 2000. Moreover, the large hadron collider (LHC) at CERN is planed to start from 2007 with higher energy, too.

In the figure 1.2, lines with arrows and points with error bars are shown.

[1]The maximum beam energy of AGS is 11 A GeV for gold ions, and one of SPS is 160 A GeV for lead ions

Lines indicate expansion trajectories of thermalized matter created in heavy–ion collisions of difference experiments. Points indicate values of temperature and baryonic chemical potential at the chemical freeze–out (circle points) and the thermal freeze–out (square points). They were measured at experiments at AGS and SPS.

On February 2000, CERN officially announced that a new state of matter (meaning quark–gluon plasma) is created there.[2] Results of their seven experiment groups (including the NA44 collaboration whose data are studied in this thesis) consists expectations to formation of quark–gluon plasma.[3]

Signatures of quark–gluon plasma in the high energy heavy collisions are proposed by several phenomenologists. J/ψ suppression is one of the most probable signature of formation of quark–gluon plasma.[4, 5] For the CERN announcement, they claimed that anomalous J/ψ suppression by measured by the NA50 collaboration implies a phase–transition reasonably.[6]

However, any candidates of every signature cannot provide a proof of the quark–gluon plasma only with itself, because quark matter in quark–gluon plasma suffers re-transition to the hadron gas state (namely confinement state) and experimenters can observe the quark–gluon plasma just indirectly. Therefore, it is necessary to investigate multiple signatures and to understand them synthetically.

The source size measurement using by the particle interferometry is also one of these signatures of the quark–gluon plasma. In this thesis it is studied using data of kaon pairs. In the next section, the particle interferometry is explained in detail.

1.3 Particle interferometry

1.3.1 Overview of interferometry

The primary property of the wave is the principle of superposition. Thus, waves interfere one another. Not only light, particles are also described as a wave function according to the quantum mechanics theory. Therefore, there could exist interference among two or more particles with the same species. The particle interferometry is a curious technique, which use the nature in the quantum mechanics.

In the 1950's, Hanbury Brown and Twiss (HBT) proposed and developed a new technique using the phenomena of intensity interference, so-called HBT interferometry.[7] This technique leads that the intensity correlations of the radiation between different detectors contain information about the spatial size of the source. They measured the diameter of the sum in 1950 at first for the demonstration of their technique, and determined the angular diameters of the radio sources *Cas A* and *Cyg A* in 1956. However, due to progress of the modern detection technique of the radio amplitudes, the Michelson interferometry has replaced to the intensity interferometry in the astronomy field.[9]

A few years later in particle physics, Goldhaber, Goldhaber, Lee and Pais (GGLP) applied the same technique (though independently developed from HBT) to pion pairs emitted from proton–antiproton collisions at the Bevatron.[8] When GGLP used the HBT technique in heavy-ion collisions at first, the shape of the correlations can be simply interpreted to source size. By the resent minute investigation, the HBT method for the heavy ion collisions has been understood that it does not directly mean the source size of the phase of quark–gluon plasma produced by the heavy ion collisions.

The radius parameters of the correlations are depends from the other effects, collective flow of the particles. In the description of the following sections, no collective flow will be assumed. Since this assumption is not realistic, the deduced radii include an effect of the collective flow.

It is similar that the other hadronic observable cannot be a direct measurement as the QGP probe, because the hadrons suffer the hadron gas phase after the phase of quark–gluon plasma if it is created. However, the source size extracted from the HBT interferometry can be interpreted as the source size (plus the effect of the corrective flow) of the hadron gas phase at the freeze–out. The QGP phase–transition affects the size of the hadron gas phase, thus it can be a QGP indirect probe.

1.3.2 Two–particle correlation function

The HBT interferometry measures the intensity correlation of the particles, instead of the amplitude interference as usual.

The HBT effect is shown in the correlation function (C_2) defined as:

$$C_2(p_1, p_2) = \frac{P_2(p_1, p_2)}{P_1(p_1)P_1(p_2)},$$

where p_1 and p_2 is four–momentum of two identical particles, $P_2(p_1, p_2)$ is the probability to measure two particles with the coincidence of momentum with p_1 and p_2, and $P_1(p)$ is the probability to measure a single particle with a given momentum p. To understand the meaning of the correlation function, we make a simple assumption as described in the figure 1.2. In this assumption, two particles (denoted as '1' and '2') have measured at the point (x_1' and x_2) with the momentum (p_1 and p_2) by the detectors, respectively. And we cannot know where they are emitted in the source. To describe the wave function of two particles, however, we will suppose the particle 1 and

particle 2 emit at x_1 and x_2. So that the wave function can be written as:

$$\psi(p_1p_2 : x_1x_2 \to x_1'x_2') =$$
$$\frac{1}{\sqrt{2}}\{A(p_1,x_1)e^{i\phi(x_1)}A(p_2,x_2)e^{i\phi(x_2)}e^{i\ p_1(x_1-x_1')}e^{i\ p_1(x_1-x_1')}$$
$$+\{A(p_1,x_2)e^{i\phi(x_2)}A(p_2,x_1)e^{i\phi(x_1)}e^{i\ p_1(x_1-x_1')}e^{i\ p_1(x_1-x_1')}\},$$

where $A(p,x)$ and $\phi(x)$ is the magnitude and phase with momentum p and point x. And it is supposed that two particles are identical species and follow the Bose–Einstein statistics, hence, the wave function is symmetry with a swap of two particles.

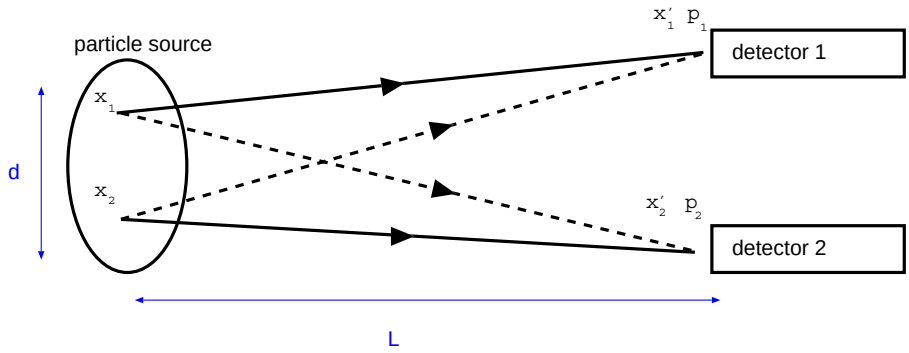

Figure 1.2: Detectors cannot distinguish the points (x_1 and x_2) where particles generate.

Since the emitted points can be not known, the wave function of the two particles which detected at the points x_1' and x_2' and the momenta p_1 and p_2, is:

$$\Psi\left(p_1p_2 : \left\{{}^{\text{all } x_1\ x_2}_{\text{points}}\right\} \to x_1'x_2'\right) = \int dx_1dx_2\rho(x_1)\rho(x_2)\psi(p_1p_2 : x_1x_2 \to x_1'x_2'),$$

where an integral is used instead of a summation, assuming the distribution of emitting points is a continuous function. The two–particle momentum distribution $P_2(p_1,p_2)$ (i.e. the probability distribution for two particles of momentum p_1 and p_2 and detection points x_1' and x_2') is:

$$P(p_1,p_2) = \frac{1}{2}\left|\Psi\left(p_1p_2 : \left\{{}^{\text{all } x_1\ x_2}_{\text{points}}\right\} \to x_1'x_2'\right)\right|^2$$

In the case of the chaotic source, i.e. the phases $\phi(x)$ are random functions of x, the integral removes the $\phi(x)$ in the wave function $\psi(p_1p_2 : x_1x_2 \rightarrow x_1'x_2')$. Then the correlation function $C_2(p_1, p_2)$ can be written as:

$$C_2(p_1, p_2) = 1 + |\tilde{\rho}(q; p_1, p_2)|^2,$$

where $\tilde{\rho}(q; p_1, p_2)$ is a Fourier transform of the density of the emitting points $\rho(x; p_1p_2)$. When the density of the emitting points can be supposed as a four dimensional Gauss function, the correlation function can be written as:

$$C_2(p_1, p_2) = 1 + \lambda \; exp(-r^2q^2),$$

where r is a four–vector of the width of the Gauss function of the source, and the q is a four–vector of the momentum difference ($q = p_1 - p_2$). And λ is the chaoticity parameter, which indicate the degree of the chaotic of the source. When the source is coherent, not chaotic, there is no correlation. That is the λ becomes unity.

1.3.3 Three–dimensional analysis

The most common three–dimensional parameterization is the Bertsch–Pratt parameterization.[12][11] The spatial three elements of the momentum difference vector $\vec{Q}$ is decomposed into a "longitudinal" direction (Q_L), an "outward" direction (Q_{TO}) and a "sideward" direction (Q_{TS}). The longitudinal direction is along the beam axis, and the outward and the sideward direction are transverse to the beam axis. The outward direction is parallel to the total transverse momentum of the pair ($p_{T1} + p_{T2}$). The schematic drawing of the Bertch–Pratt coordinate system is shown in the figure 1.3.

The correlation function for the three dimensional analysis using the Bertsch–Pratt parameterization are written as:

$$C_2(p_1, p_2) = 1 + \lambda \; exp(-R_L^2Q_L^2 - R_{TS}^2Q_{TS}^2 - R_{TO}^2Q_{TO}^2),$$

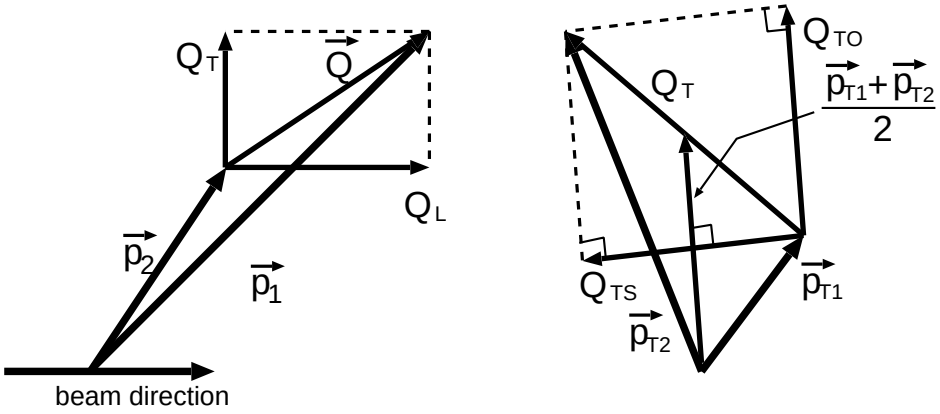

Figure 1.3: The Bertsch–Pratt coordinate system used for three dimensional correlation function.

where R_L, R_{TS} and R_{TO} are the longitudinal, outward and sideward radius parameter, respectively. An image of these radius parameters is drawn in the figure 1.4.

This parameterization allows us to measure the longitudinal size, the transverse size, and the duration time of the source. The sideward radius parameter (R_{TS}) is thought to measure the transverse size of the source, while the outward radius parameter (R_{TO}) couples the transverse radius with the duration time of the source.

The reference frame for making the correlation function is used the "longitudinally co-moving system" (LCMS[2])[14], which is defined as the center–of–mass frame of the pair ($p_{z1} + p_{z2} = 0$) for the longitudinal direction and the center–of–mass frame (i.e. the laboratory frame) of the projectile and target nuclear for the transverse direction. When the LCMS frame is used, the difference between the outward radius parameter (R_{TO}) and the sideward radius parameter (R_{TS}) can be analytically deduced as the relation of the

[2]The LCMS is sometimes written as an acronym of the Longitudinal Center of Mass System.

duration time ($\Delta\tau$) and the transverse flow velocity of the pair β_T, i.e.:

$$R_{TO}^2 - R_{TS}^2 = (\Delta\tau\beta_T)^2$$

That means the important property which the duration time can be reduced from the three–dimensional analysis of particle interferometry.

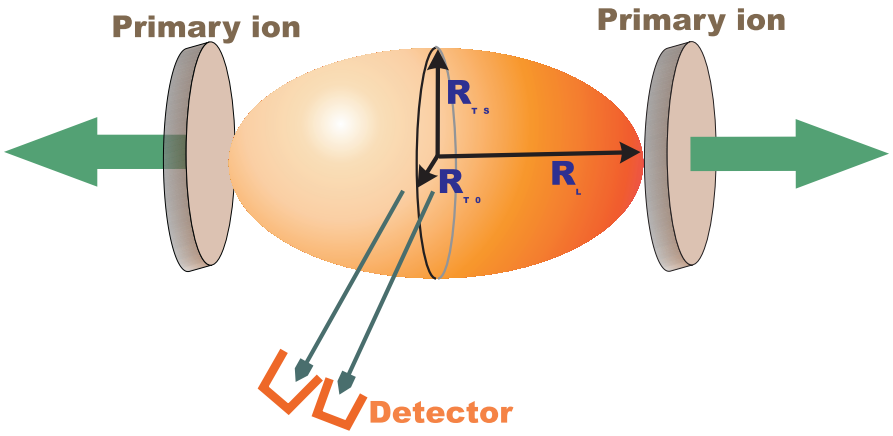

Figure 1.4: A sketch shows R_L, R_{TO} and R_{TS} in the Bertsch–Pratt parameterization.

1.3.4 One– or two–dimensional analysis

For most of the conventional measurements, a parameter of the invariant momentum difference (Q_{inv}) are used for making the correlation function, because of the low statistic of the pairs and the convenience of the independent to the coordinate system. The invariant momentum difference is defined as:

$$Q_{inv} = \sqrt{\left|\vec{Q}\right|^2 - \Delta E},$$

where $\Delta E = E_1 - E_2$ and the $\vec{Q}$ is the three–vector of the momentum difference. The one–dimensional Gaussian parameterization can be written as:

$$C_2(Q_{inv}) = 1 + \lambda\, e^{-Q_{inv}^2 R_{inv}^2},$$

where R_{inv} is the invariant radius parameter. Since the correlation function and Q_{inv} is invariant of the Lorentz transform, the measured invariant radius parameter is also independent to the choice of the coordinate system. It can be useful for the comparison of the results among different experiments. The invariant radius parameter is enough for rough discussion of the source size, but it has no intuitive physical meaning. For the detail investigation of the particle source, the three–dimensional analysis becomes important.

The two–dimensional analysis is developed by the NA44 collaboration, because of the limitation of its acceptance for the momentum difference. The correlation function for the two–dimensional parameterization is done using a function:

$$C_2(Q_L, Q_T) = 1 + \lambda\, e^{-Q_L^2 R_L^2 - Q_T^2 R_T^2},$$

where Q_L, Q_T are the longitudinal and the transverse momentum difference respectively and R_L, R_T are correspond radius parameter. This parameterization assumes symmetry between the sideward and the outward for the three–dimensional analysis. So that the three–dimensional analysis is better for the detail investigation, but it is true that the two–dimensional parameterization has more information than the one–dimensional parameterization.

1.4 Kaon interferometry as a QGP probe

Since the mid-1950s, the technique of the particle interferometry has been extensively used to study the source size for particles emitted from various reactions. It usually used the pions, which are dominantly emitted in the nuclear collisions.

In the late-1980s, Scott Pratt found an long breakup time of a particle source after the formation of a quark-gluon plasma in high energy heavy

ion collisions, because initial entropy is larger by a factor of $(37/3)^{1/4}$ and it is conserved on reentering to the hadron gas phase.[12] It is assumed the formation of the quark–gluon plasma is the first order phase transition.

Experimentally, the pion interferometry data of the NA35 experiment[25] at CERN/SPS can be explained by the hydrodynamical model[15] for central O + Au collisions, and the unusual long breakup time.

For the interferometry results of the later experiments, the NA44 experiment[41, 38], the NA49 experiment[17] and the WA98 experiment[18], however, no enormous long duration time has been found.

The kaon interferometry as signal for the phase transition has been proposed and studied for the long term.[19, 20, 21, 22] There are some interest points for the kaon interferometry rather than the pion interferometry. First, the cross section of K^+'s in the hadron gas is significantly smaller than that for pions, and thus kaons may view a different stage of the collisions process. Second, the production of K^+ for the ultra–relativistic heavy ion collisions could be enhanced. It is theoretically known as the "strangeness enhancement". Finally, the correlation of kaons is not affected from the long–lived resonance decay.

Hence, the kaon interferometry can serve as a valuable complementary probe of the space–time geometry of nuclear collisions, even though the disadvantage of kaon interferometry is, i.e. it is necessary that higher statistics by about one hundred times. The production ratio of kaon pairs to pion pairs is around $(N_K/N_\pi)^2 \sim 1/100$.

Chapter 2

Experiment

2.1 The NA44 experiment

The NA44 experiment[23] is one of the second generation experiments at the CERN/SPS. The NA44 experiment is operated by an international collaboration organized in 1989, consisted of more than 50 members from 12 institutes.[1]

A focusing spectrometer was constructed to measure identified secondary particles from heavy ion collisions with good momentum resolution at mid–rapidity region, in order to study the distributions of single–particles and multi–particles.

The original motivation of this experiment was that NA35 experiment at CERN reported a large hadron source in the O+Au collisions.[25] Since the large source sizes was predicted as the QGP signal, it was getting interest to study a hadron source size in more details. The NA44 experiment was proposed to measure particle correlations in 1988, aiming to study the geometrical source size and its shape with good accuracy, using by the HBT method.

[1] The more information and the resource of NA44 available on the World–Wide–Web: `http://www.nbi.dk/na44/`.

2.2 Accelerator and heavy ion beam

The high energy heavy ion beam is supplied from the Super Proton Synchrotron (SPS). The SPS is located at the European Organization for Nuclear Research (CERN) on the border between France and Switzerland near Geneva. The SPS has a large ring (circumference is 6.911 km) and 744 bending magnets with 2 T. Because of an RF limitation of a synchrotron, the injection ions need to be pre–accelerated to enough energy before. Such the acceleration system (so call accelerator complex) consists of several accelerators.

The schematic drawing of the accelerator complex is shown in figure 2.1. At first, the heavy ions stripped of the outer electrons in the electron cyclotron resonance ion source (ECR) are accelerated in a linear accelerator (LINAC3) until 4.2 MeV of energy per nucleon. They pass a stripping foil, and then are injected into the PS booster (PSB) ring. In this ring, the ions are accelerated up to 94.4 MeV per nucleon, and they are transported to the proton synchrotron (PS). After the ions are accelerated to 5.1 GeV per nucleon in the PS, they are injected into the super proton synchrotron (SPS). In the transfer line from the PS to the SPS, the ions are fully stripped. After acceleration at the SPS, the ions reach the final energy. For the lead ion, the energy is reached to 158 GeV per nucleon, and 200 GeV per nucleon for sulphur ion and 450 GeV for proton. The maximum energy per nucleon is limited by the strength of the magnetic field, and related with a specific charge (i.e. Z/A) of heavy ion.[2]

The heavy ions are extracted from the SPS, and are transported through the high intensity H4 beamline to the NA44 spectrometer. The NA44 spec-

[2]For the $e^+ + e^-$ experiment in the high energy particle physics, the SPS and other accelerators is used as the pre–accelerator of the LEP, and will be used for the LHC.

trometer is located at the north experimental hall in Prevessin, France. The beam rate in the H4 beam line can be controlled. For lead ion running, the typical beam intensity was 3×10^6 ions in 2 second spill with a intermission of 3 seconds, which corresponds to 0.6×10^6 ions per second.

2.3 The NA44 spectrometer

The NA44 spectrometer was designed to measure identified two–particle correlations with good momentum resolution. Figure 2.2 shows the schematic view of the spectrometer. The momentum measurement uses an orthodox method of a particle spectrometer, which measures a bending angle of particle trajectories in static magnetic field. Two dipole magnets (hereafter abbreviated as D1 and D2) provided the magnetic field. To find out the particle trajectories, a suit of tracking detectors, consisting of a pad chamber (PC), two strip chambers (SC1 and SC2) and three plastic scintillator hodoscopes (H2, H3 and H4), is employed. The spectrometer can be rotated around the target position, in order to measure in a different kinematic region. The particle identification (PID) is carried out with a combination of information from the threshold type Cherenkov counters (C1, C2, TIC) and the time of flight (TOF) measurement between the Cherenkov beam counter (CX) and the hodoscopes (H2, H3 and H4).

2.3.1 Target and detectors around the target

Several targets with different thickness were prepared. For the two–kaon correlation measurement with the Pb beam, we chose a 3 mm thick lead target. This material corresponds to 3.1×10^{-2} of the collision length.

To detect nuclear collisions, we have installed two Cherenkov beam counters (CX1 and CX2), a beam veto counter (CX veto), a scintillation multi-

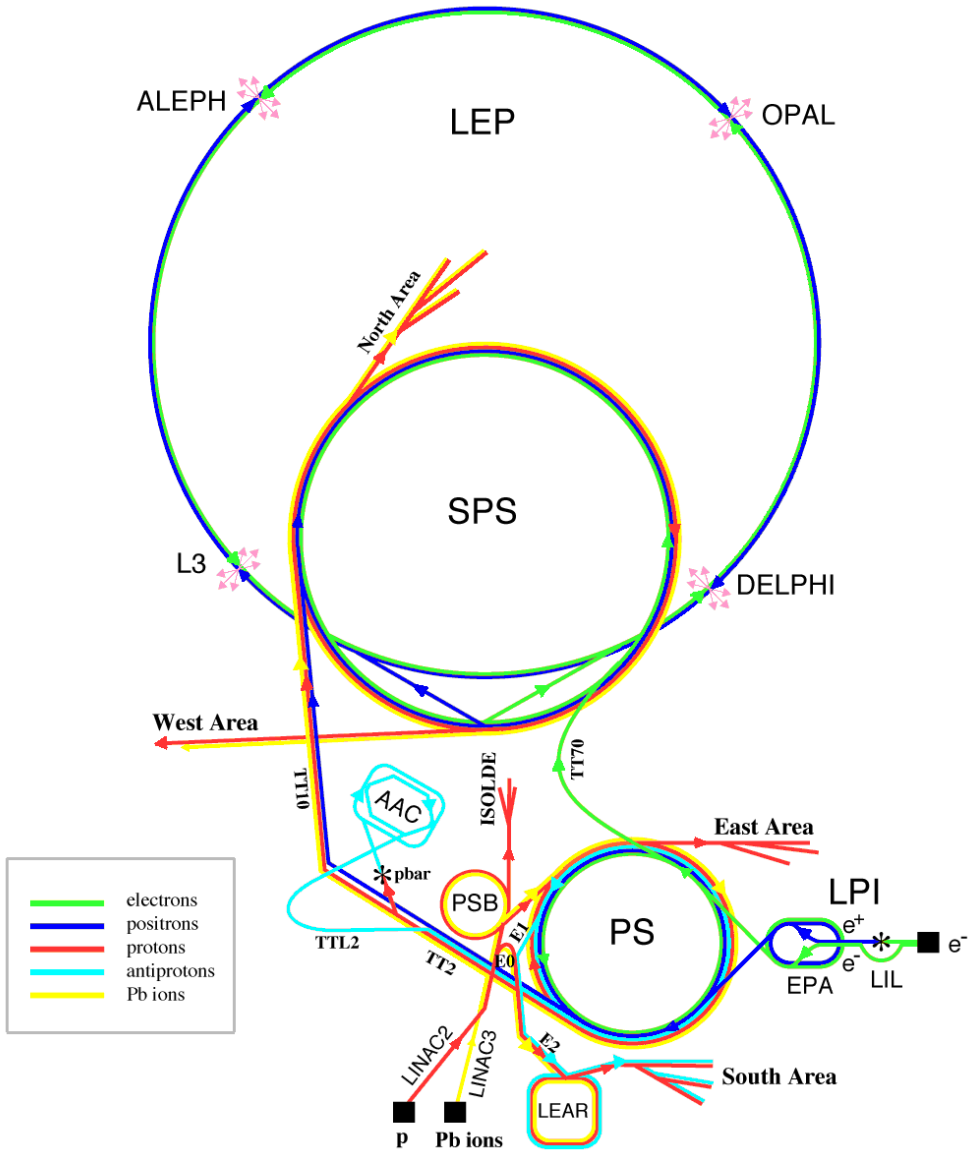

Figure 2.1: CERN accelerator complex. The NA44 spectrometer is set at the north area.

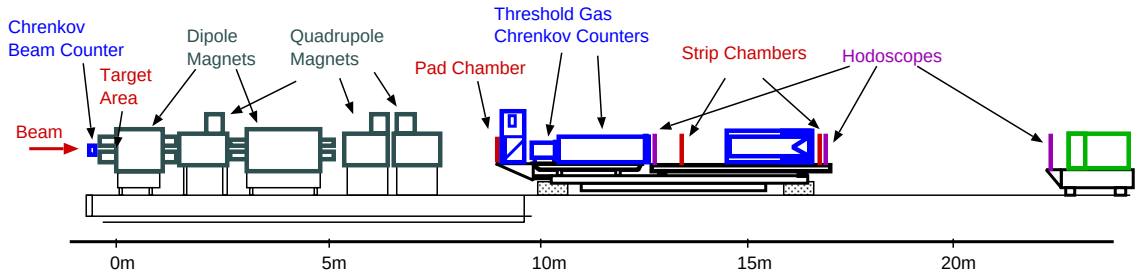

Figure 2.2: Setup of the NA44 focusing spectrometer for Pb+Pb collisions.

plicity counter (T0) and a silicon pad counter (Si) around the target. (See figure 2.3.) Information of these subdetectors is used to reject backgrounds (double collisions, beam halo, beam–gas collisions and low multiplicity collisions) and to measure the start timing of TOF by CX.

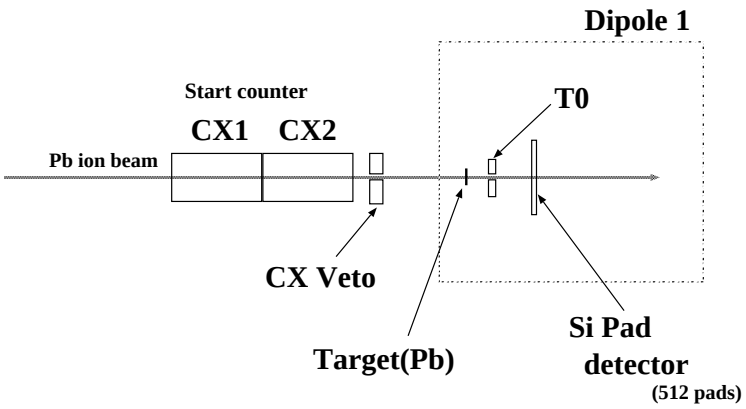

Figure 2.3: Configuration of the target region.

CX consisting of two gaseous Cherenkov counters (CX1 and CX2) filled with nitrogen gas, is located at 50 cm upstream of the target.[26] The radiator lengths are 15.5 cm and 20.5 cm for CX1 and CX2, respectively. It detects the incident beam ions. Since the number of Cherenkov photons is proportional to the square of the electric charge of the beam nuclei, it produced a large pulse than background particles, since the beam halo or secondary particles produced upstream in a beam line may have lower atomic number. The

CX veto's are also installed to reject the background. The CX veto is the scintillation counter, and is located downstream of the CX counters. The scintillator has a hole of 5 mm radius on the beam line. The signals of CX1 and CX2 are sent to the trigger logic in order to define a collision. Pulse height of signals of the CX counters is presented a number of incident ions in an integrated period. Figure 2.4 shows a distribution of pulse height of CX1 and CX2. The first peak at the lower pulse height shows events of single ion injection during the ADC gate. The second and the third peak indicate two and three ions entered together in the period, respectively.

CX also has a role as the start counter of the time–of–flight (TOF) measurement. The figure 2.5 shows a distribution of the time difference between the CX1 and CX2. The fluctuation of time difference shows the quadratic sum of the uncertainty of time measurement by CX1 and CX2. Assuming CX1 and CX2 have the same timing resolution, each resolutions was evaluated from the sigma of the time difference to be 30ps. This value is very good enough to identify particle species using TOF. Please see the later description about the particle identification.

The scintillation multiplicity counter (T0) is used to measure the start timing of TOF in case of the proton beam, because of lack of Cherenkov light in CX for proton beam. For the heavy ion runs, the T0 counter did not provide the start timing, but measured a multiplicity of charged particle for event characterization . This consists of two scintillator panels with a small gap across the beam line. On the top and the bottom sides of each scintillator, a light guide and a PMT are mounted. This is closest to the target, about 1.0 cm downstream from the target. This covers pseudo–rapidity from 1.3 to 3.5. Since this detector uses the PMT technique, the data can be quickly read out and used as the trigger to select the centrality. For the heavy ion

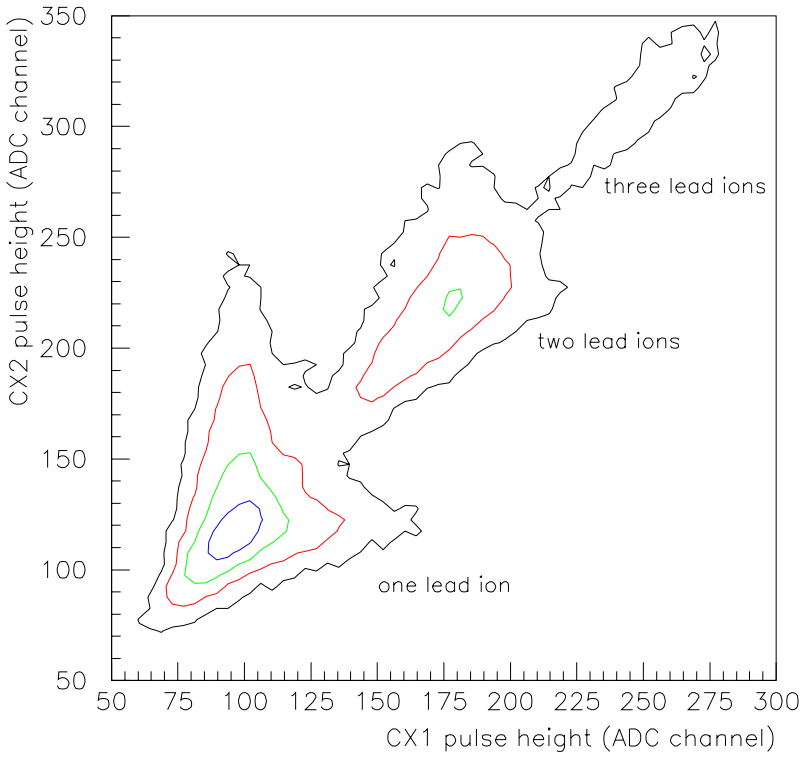

Figure 2.4: The pulse height distribution of two beam counters (CX1 and CX2). The first peak shows that single ion incidents on the target during an ADC gate. The second peak shows two ions are injected. In this analysis, only the first peak is selected to reject double collisions. The contour lines logarithmically increase.

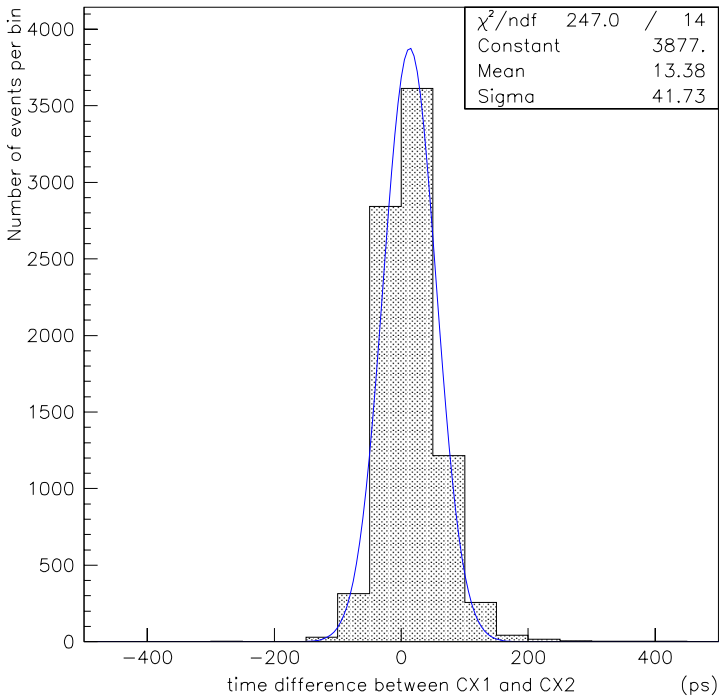

Figure 2.5: The time difference of the two beam counters (CX1 and CX2). The zero point on the abscissa is taken arbitrarily. The fluctuation of difference (about 42ps) comes from the intrinsic resolution (about 30 ps) of each counter.

run, the primary beam emits many δ–electrons, which become background for the T0 detector. Since the target area is in a magnet field and the δ–electrons have relatively low energy, they are swept out to one side by the magnetic field. The data in the opposite side is used to deduce the centrality.

The silicon pad detector (Si) provides the multiplicity of charged particles in a heavy–ion collision as the number of hit segments for the supplement of T0 counter. The pseudo–rapidity coverage is $1.5 < \eta < 3.3$. The silicon detector is a disk of 0.3 mm thickness with a hole of 4mm diameter at the center. It is divided to 32 segments in angle, and radially into 16 segments, and then 512 pads in total. In the radial direction, the segmentation is made to provide even equal width in the rapidity range. The pulse height is used to correct the effect of multi–hit on a pad. This is also affected by the δ–electrons, then we use only the δ clean side to decide the multiplicity. The readout from the silicon detector is relatively slow, so that we used it only in the offline analysis.

2.3.2 Dipole and quadrupole magnets

Electromagnets are important components for the NA44 spectrometer. We have two dipole magnets (D1 and D2) and three quadrupole magnets (Q1, Q2 and Q3). A target is placed at the upstream edge of D1 with a 1 m length. D1 serves to separate the secondary particles from the primary beam, which enters a beam dump.

The secondary particles are transported to the series of super–conductive quadrupole magnets (Q1, Q2 and Q3). The purpose of quadrupole magnets is to make a large acceptance in one plane and reduce the acceptance in the other planes. Then we need two focusing configurations. One is the horizontal setting which focuses tracks in a horizontal plane onto the pad cham-

ber which defines particles. The other is the vertical setting which focuses tracks in a vertical plane at the hodoscope detector downstream. Normally, the horizontal setting is used because the Monte Carlo calculation shows a better momentum resolution than that of the vertical setting. The three-dimensional analysis of HBT technique, however, requires the acceptances of the both directions.

Between Q1 and Q2, another dipole magnet (D2) is installed. This magnet assists to bend the secondary particles. By adjusting the magnetic fields of D1 and D2, we can select the momentum range of secondary particles going to the tracking detectors. For the lead on lead runs, the data were taken for the nominal momentum settings of 4 GeV/c, 6 GeV/c and 8 GeV/c.

2.3.3 Tracking arm

To measure the tracks of the multi–particles, a pad chamber (PC), two strip chambers (SC1 and SC2), three scintillation hodoscopes (H2, H3, H4) are installed. Moreover, an aerogel Cherenkov counter (ACC), multi–particle threshold imaging Cherenkov counter (TIC) and threshold gaseous Cherenkov counter (C1 and C2) are installed for the particle identification. A uranium calorimeter is also install to help anti–baryon identification. These detectors are placed on a line, and it can be moved at different angles from the primary beam axis to cover a broad transverse momentum range. Two angular settings were used, a small angle setting at 44 mrad (for low transverse momentum measurement) and a large angle setting at 131 mrad (for high transverse momentum measurement).

Tracking chambers

As it is shown in the figure 2.2, a pad chamber (PC) and two strip chambers are installed after and before the Cherenkov counters. The first detector in the spectrometer arm is the PC located at 9 m from the target after the Q3 magnet. The size of the pad chamber is 130 mm (horizontal) $\times$ 220 mm (vertical). The pad chamber contains a multi–wire proportional chamber (MWPC) with horizontal wires and two cathode planes which are segmented in 576 (32 $\times$ 18) pads. The pad size is 4 mm (horizontal) $\times$ 12mm (vertical). The wire pitch is 3 mm, so that each pad collects charge from 4 corresponding wires. The two pad planes are shifted by 2 mm (a half length of pad) in the horizontal and 3 mm (a quarter length of a pad) in the vertical, to improve the hit position resolution. The wire signals are read out and can be used in the trigger. For the correlation data, the pad chamber is a part of the trigger which requires two tracks in the spectrometer at least. This allows us to take data very efficiently.

SC1 and SC2 are located at about 14 m and 17 m downstream from the target, respectively. The two tracking chambers are identically designed. Their size is 76 cm (horizontal) and 25 cm (vertical). They consist of two independent subchambers of a vertical chamber (SCV) and a horizontal chamber (SCH). The horizontal chamber has vertically aligned wires and horizontally aligned strips. For the vertical chamber wire and strip orientation is the opposite. The number of strip is 256 and 384 for SCH and SCV.[28]

Scintillation Hodoscopes

The time of flight (TOF) measurements are performed by the three hodoscopes H2, H3 and H4 which are positioned at 14 m, 18 m and 24 m from target. All hodoscopes are similar in construction and differ only in

size and the segmentation.[29] They are made as a wall of vertically aligned plastic scintillator slats. In the table 2.1, the hodoscope specifications are summarized. Because the secondary particles are diffused as going to downstream, the H4 is designed as the largest subdetector. On each side of a slat, a photo–multiplier tube (PMT) is mounted. The signals of PMTs are measured for the timing (by TDC modules) and pulse charge (by ADC modules). The timing resolution of TOF, σ_{TOF}, is around 100 ps. The hit position in the horizontal direction is given by the slat position. The vertical position is calculated from the time difference between the top and bottom timings of PMT signals in a given slat. In order to calibrate this vertical position, three horizontal scintillator slats (called finger counters) are mounted across the hodoscopes. The signals from H2 and H3 are used in the trigger for the spectrometer multiplicity equals to 1 (MUL1) and 2 (MUL2). The trigger is described in latter.

Table 2.1: The specification of the NA44 scintillation hodoscopes.

	H2	H3	H4
Number of slats	60	50	60
Distance from target (m)	13.9	18.35	24.60
Slat length (cm)	20.0	22.0	70.0
Slat width (cm)	0.6	1.3	2.3
Slat thickness (cm)	0.6	1.0	2.2
Horizontal position resolution (cm)	0.18	0.38	0.66
Vertical position resolution (cm)	0.8	0.7	0.8
Timing resolution (ps)	130	95	95

Threshold gaseous Cherenkov counter

The threshold gaseous Cherenkov counters (C1 and C2) consist of a radiator gas tank and a mirror, which reflects the emitted light into a phototube

mounted at the side of the tank. The particles passing through C1 and C2 are nearly parallel to each other, therefore their Cherenkov light can be focused on a window of a PMT.

To discriminate particles traveling with a faster velocity from other slow particles, a threshold velocity is set below these faster particle of interest. Adjusting a gas pressure, the index of refraction can be changed, that is changing the velocity of the light in the gas. For the real operation, two pressure settings named "low" and "high" pressures were used. C1 was filled with freon 12, with the aim to discriminate between π, K and p depending on the pressure and the momentum setting of the spectrometer. C2 was filled with nitrogen/neon and its main purpose was to veto electrons. The specifications of the Cherenkov counters are given in the table 2.2. Information of C1 and C2 are used in the trigger for online particle identification. This function is extremely important to enrich a kaon probability in the data sample.

Table 2.2: Threshold momentum for C1 and C2, in GeV/c.

	electron	pion	kaon	proton
C1 (=1.4 atm)	0.0	2.5	8.9	16.9
C1 (=2.72 atm)	0.0	1.8	6.4	12.1
C2 (=1.0 atm)	0.0	6.5	23.0	43.7
C2 (=1.3 atm)	0.0	5.2	18.3	34.8

Multi–particle threshold imaging Cherenkov counter

The multi–particle threshold imaging Cherenkov counter (TIC) [30][31] was designed to provide a track–selective π/K separation in the 3–8 GeV/c range. The schematic view of TIC is shown in the figure 2.6. TIC was installed for the lead beam runs, which started in 1994, because we have no track–

associated information from C1 nor C2 and the lead on lead collisions have higher particle multiplicity than those of sulphur on lead reaction. Cherenkov photons created in an isobutane radiator with 1 m long at the atmospheric pressure are reflected to the top and bottom of the detector by a pair of flat mirrors. The Cherenkov threshold momentum is 2.2 GeV/c for pions and 7.9 GeV/c for kaons. Photons are detected in pad chambers on the top and bottom detector after the photons are converted to electrons by a coated layer of CsI on the cathode plane.

The figure 2.7 shows a contour plot of the mass–square from the TOF versus the number of hit pads associated with a given track, which has about 4 GeV/c momentum. A clear separation of pions and kaons is possible.

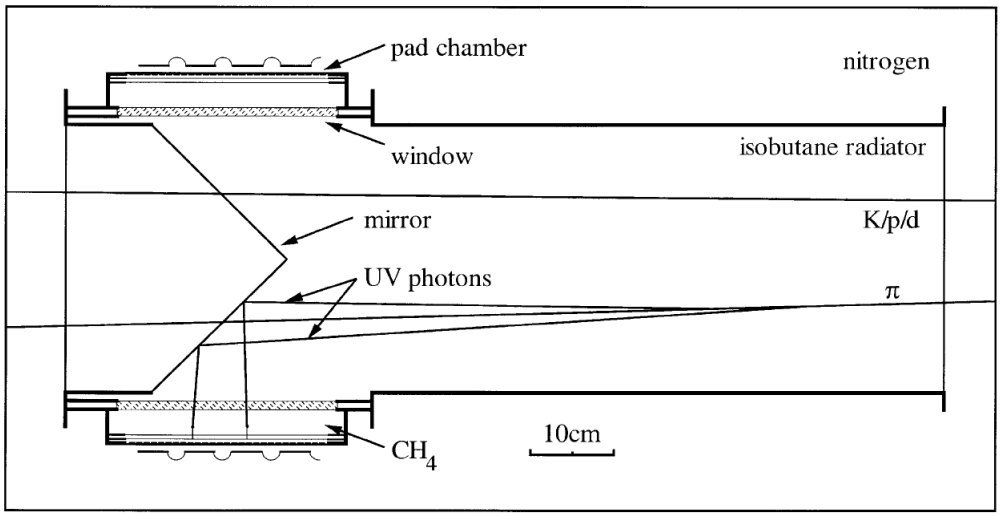

Figure 2.6: The side view of the TIC.[30].

Aerogel Cherenkov counter

The aerogel Cherenkov counter (ACC) can identify particles track by track like as the TIC by measuring the image of Cherenkov light. Moreover, the

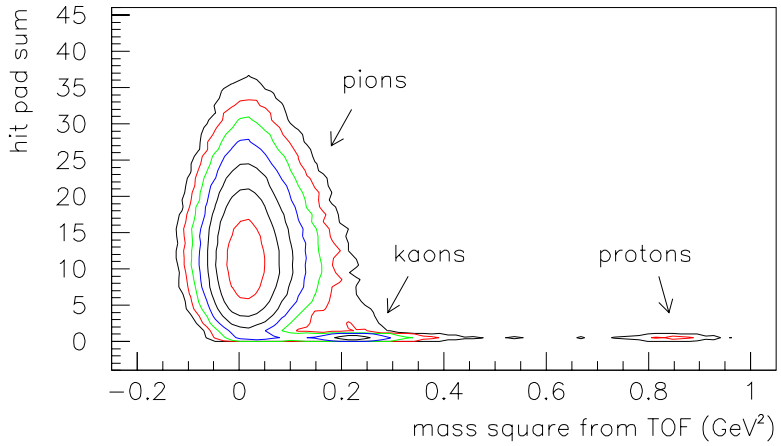

Figure 2.7: Contour plot of the mass–square versus number of hit pads of each track in the TIC. Pions and kaons can be clearly separated.

information of ACC could be used as the trigger. However, this detector was not used for the real operation. For more detail, see [32].

Uranium Calorimeter

The uranium calorimeter (UCAL) is located at the end of the spectrometer, 24 m downstream of the target. Since UCAL measures the total energy of annihilating anti–particles, it is used for $\bar{p}$ and $\bar{d}$ identification.[33]

2.3.4 Data acquisition and Trigger system

Since 1995 NA44 used a data acquisition system (DAQ) based on the CASCADE environment, which was developed and supported by the CERN computing group. The signals from the detectors are read out via either CAMAC or VME based CRAMS. An event is processed in 6 ms. The readout for CAMAC takes 3 ms, CRAMS readout takes about 1 ms and about the data

packing in the CASCADE takes about 2 ms. The size of a typical event is about 5–8 kb.

There are several kinds of triggers, which come from the corresponding detectors. The trigger signals are created in the experimental zone with NIM logic modules connected to these detectors . These logic signals are sent to the counting house where they are combined according to the appropriate trigger for the appropriate data. (See figure 2.8.)

The trigger components used are summarized in the following list:

Valid beam (VB)

This requires a good signal from CX, but no signal from the CX veto counter. (i.e. VB = CX $\cap$ $\overline{\text{VBC}}$) The valid beam is required for all runs.

Centrality (T0)

An analog signal from T0 is used for the centrality trigger. In case of small T0 threshold, events require only an interaction of projectile nucleus and target nucleus.

Track (MUL1, MUL2 or MUL3)

Particles in the tracking section are defined by H2 and H3. A single track trigger (MUL1) is defined as a good signal in a single slat of both H2 and H3. A pair track trigger (MUL2) requires two hits on each hodoscope. To take the data for the HBT analysis, the MUL2 was usually required. The MUL3 is a similar definition, requires three–hits on each hodoscope. The signals of the pad chamber and H4 can also be required for more stringent trigger.

Particle identification (C1 and C2)

Using the signals of C1 and C2, species of the secondary particles can

be selected. The selected species depend on the pressure of the gas in C1 and C2. The requirement can be set either *require*, *veto*, *ignore*.

The data are taken with a mixture of trigger settings at different scale–down factors. For example, the data used in this thesis were taken by the trigger with $\mathrm{VB} \cap \mathrm{T0} \cap \mathrm{MUL2} \cap \overline{\mathrm{C1}} + \overline{\mathrm{C2}}$ and $\mathrm{VB} \cap \mathrm{T0} \cap \mathrm{MUL3}$ (C1 and C2 are ignore). For the later trigger setting, the data was taken only an event every 16 events.

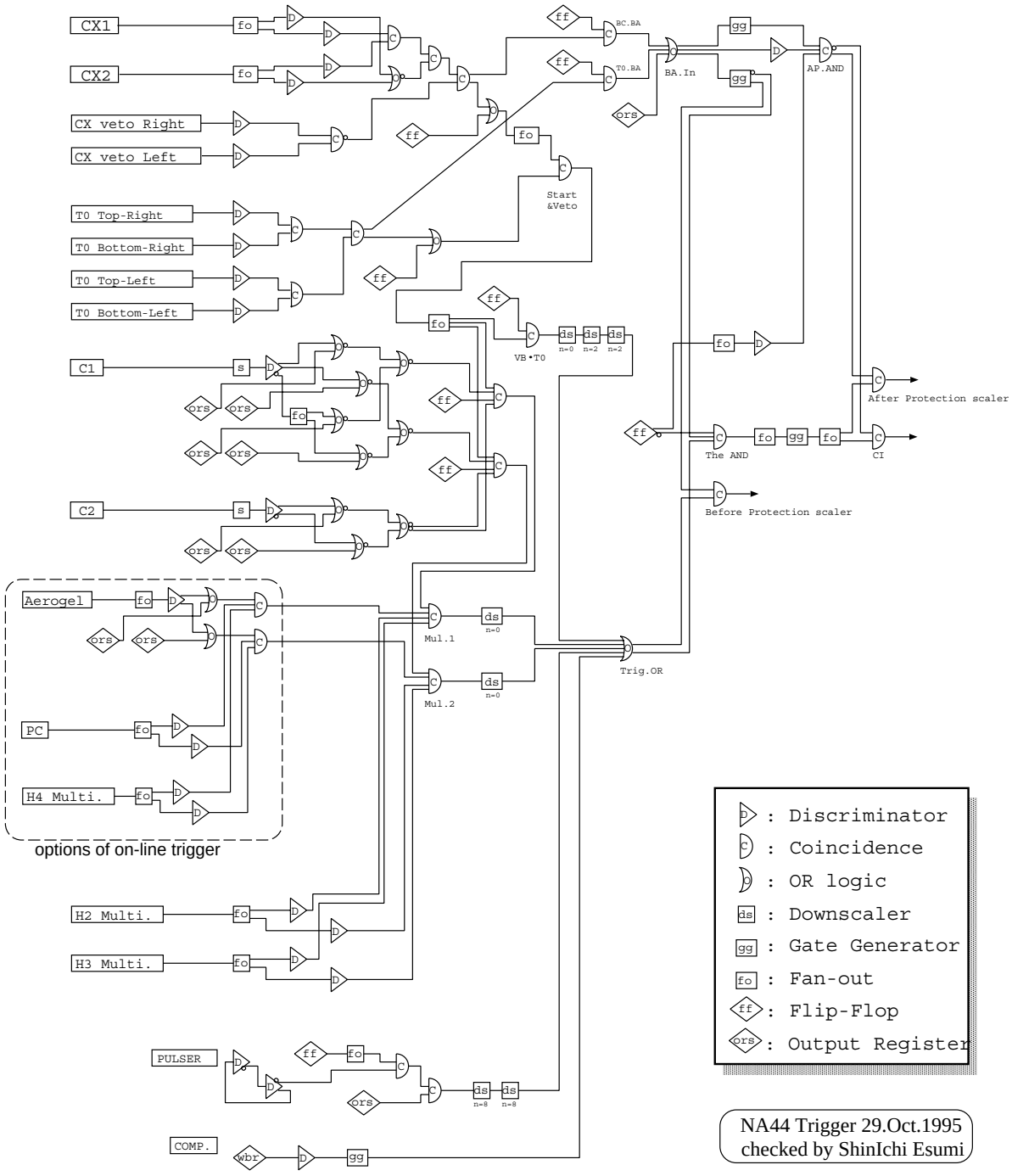

Figure 2.8: Logigal diagram of the NA44 trigger.

Chapter 3

Data and analysis

The analysis to deduce correlation functions and to extract source parameters can split into several steps. In the first step, the raw data, which is collected by the NA44 apparatus and the DAQ system, is corrected for various distortions. Since the raw data are recorded as digitized in instrumental units of the ADC and TDC modules, the data are calibrated into values in physical units.

After the calibration of data for every detector, tracks of secondary particles are reconstructed from the hit information for each detector, and the momentum for each track is calculated from the bending angle in the magnetic field. These extracted values are stored in a DST[1] file with information for each event. All the NA44 physics analyses based on the common DST files. Based on this file, event selections and particle identification are performed. After those, the correlation function is extracted. The correlation function suffers distortions from the Coulomb repulsion and the spectrometer acceptance. To evaluate and correct for these distortions, MC simulations are employed. Finally, corrected correlation functions are fit using a Gauss function and source parameters are deduced. The systematic errors are estimated

[1]DST is an acronym of "data summary tape".

for the extracted results.

3.1 Calibration and reconstruction

Calibration processes are mainly performed by using data itself. However, some special runs are dedicated to specific sub–detectors. The all calibration constants are stored in a calibration database and read out by the track reconstruction program.

3.1.1 Calibration of hodoscopes

The hodoscopes measure hit positions and arrival times of each particle. The horizontal hit positions are determined by the slat position, while the vertical hit positions are calculated from the time difference of the pulses between the top and bottom PMTs on each slat. The hit time is defined as the average timing of the pulses of in each PMT. Thus, it is important that the timing resolution of PMTs. The timing of PMT pulse measured by a typical leading–edge discriminator has time delay depending on the pulse shape. The slewing correction is to correct this time delay using the information of the pulse height measured by ADC modules.

The timing value of a PMT pulse measured by a TDC module has an offset value. Thus, the hit timing and the vertical position have random offsets for each slat. To measure timing offsets, finger counters are installed. Requiring a hit at the finger counters, the vertical position was directory found. The offsets of the vertical hit positions from the timing difference are subtracted from the position observed. Since the hit time is used for the calculation of mass, the offsets of hit timing are decided in a part of calculation.

3.1.2 Calibration of chambers

Two calibrations were done for the pad chamber and the two strip chambers. The first one is a correction for nonlinearity and gain of the readout electronics. Since these effects depend on hardware, it is done only once unless there was a hardware change. The second one is a correction for noisy readout channels. It is basically done for each run.

3.2 Track reconstruction – DST production

Once the calibration for raw data is completed, the track can be reconstructed. Therefore, momentum, mass–squared and other information related with a track can be determined using the corrected information of sub–detectors. This process is done by a reconstructing program called "NA44DST". This program makes a DST file. The DST file, which is an ntuple–format file of CERNLIB, contains the calibrated data, the scaler information, the hit positions and reconstructed variables (momentum, mass–squared and so on) for every event.

It stores the status of all the sub–detectors for every event, and information of the pad chamber and the hodoscopes (horizontal and vertical position and the hit time on the hodoscopes) for every channel of every event. The information related with reconstructed track is also stored, which includes two dimensional hit position and hit time on tracking detectors, and three dimensional momentum, rapidity (assuming that the track came from a pion, a kaon, a proton or a deuteron), and mass–squared (calculated from the momentum and the time–of–flight on the hodoscopes), the information of the TIC and the chi–squared value (χ^2) and confidence level (C.L.) in horizontal and vertical direction for each track.

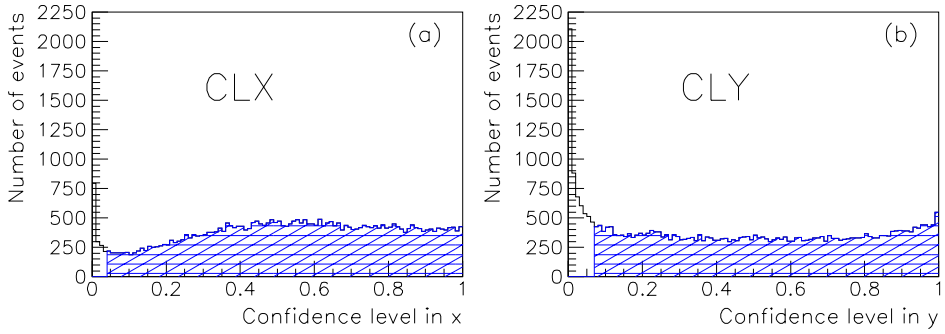

Figure 3.1: The histogram of the confidence level in x and y direction. The hatched area shows a region used the analysis.

Tracking detector hits with low ADC values are removed and bad channel of chambers are disregarded. Then a valid track is defined as a track which has hits in the pad chamber, H2, H3 and three (at least) of the four wire planes in the two strip chambers. A straight line is fitted to the hits requiring minimum chi–squared. For quality assurance of the track, a statistical confidence level of fitting is evaluated for both horizontal and vertical direction. The confidence level is defined as the probability of getting a χ^2 greater than given value which depends on the degrees of freedom.

By fitting hit positions on H2 and H3, the momenta of tracks are determined. To make momentum reconstruction quick, tracks in the spectrometer have been simulated with a program called DECAY TURTLE, where charged particles are followed through the magnetic fields, and look–up tables were created from the momentum of simulated particle and the hit positions on the hodoscopes. From those look–up–tables, a correspondence between hit positions on H2 and H3 and a momentum on a particle are parameterized by a polynomial function in each spectrometer configuration (i.e. spectrom-

eter angle, field of dipole and quadrupole magnet). Thus the momentum of a reconstructed track can be calculated as a polynomial function of the horizontal and vertical position on H2 and H3, with the coefficients of the polynomials depending on the spectrometer configuration.

For the particle identification, the mass of a reconstructed track (particle candidate) is important information. The mass–squared of a track (m^2) is calculated from the time–of–flight (T_{TOF}), path length (L_{path}) and reconstructed momentum (p) as the following formula:

$$m^2 = p^2 \frac{1-\beta^2}{\beta^2} \tag{3.1}$$

$$\beta = \frac{L_{path}}{T_{TOF}}, \tag{3.2}$$

where β is the velocity of the particle. The L_{path} is a given length between each hodoscope from the target. Because the aperture where secondary particles travel in the NA44 spectrometer is very narrow, the difference of each trajectory length for the L_{path} is negligible. The T_{TOF} is defined as the difference of hit time between the CX and the hodoscopes. Since there are three hodoscopes (H2, H3 and H4), three values of mass–squared can be calculated. The mass–squared from H3 hit time are always used because of the good timing resolution. Because the hit time of every slat of hodoscopes has an intrinsic time offset, the T_{TOF} has a time offset for each slat, too. These offsets are adjusted in the calibration process to make a single peak in the mass–squared distribution for a particle of interest. These offsets were determined in slat–by–slat for each dataset. Because our spectrometer has finite time resolution, velocity of particles (β) could be beyond 1, and the value of mass can be imaginary, so the mass–squared (m^2) are stored in DST instead of mass (m).

3.3 Dataset

In this analysis, we have three datasets in the Pb+Pb collisions. Two datasets are taken with the small angle configuration of the spectrometer (i.e. low transverse momentum $\langle p_T \rangle \sim 250$ MeV/c) for the horizontal and vertical settings of the quadrupole magnets in the fall of 1995. The other is the data of the large angle configuration for a high transverse momentum ($\langle p_T \rangle \sim 910$ MeV/c, which was taken in the fall of 1996. These datasets are summarized in the table 3.1.

In these datasets, two kaon–track candidates are included in the mid–rapidity and of a transverse momentum region given by the spectrometer setting. The plots (a), (b) and (e) in figure 3.2 show the acceptance for each setting in transverse momentum (p_T) and rapidity. The data of the horizontal setting has good momentum resolution, but it has very narrow acceptance of the Q_{TS} which is the key component of momentum difference for the three–dimensional analysis. (Please see the section 1.3.3 for the coordination of the momentum difference.) Therefore, another measurement with the vertical setting is performed for the small angle setting. The acceptance of momentum difference in each dataset is shown in figure 3.3.

For the small angle setting, an aperture is installed. The shape of jaws are different between for the horizontal and vertical settings, as shown in figure 3.4. A role of jaws is to reduce particles enter to the spectrometer. The reduction of particles are important because a possibility that an event has a pion at least becomes bigger, and the kaon trigger by C1 and C2 excludes these events.

For the large angle setting, data are not taken with the vertical quadrupole setting because of the limited Pb beam time. So we applied this dataset only

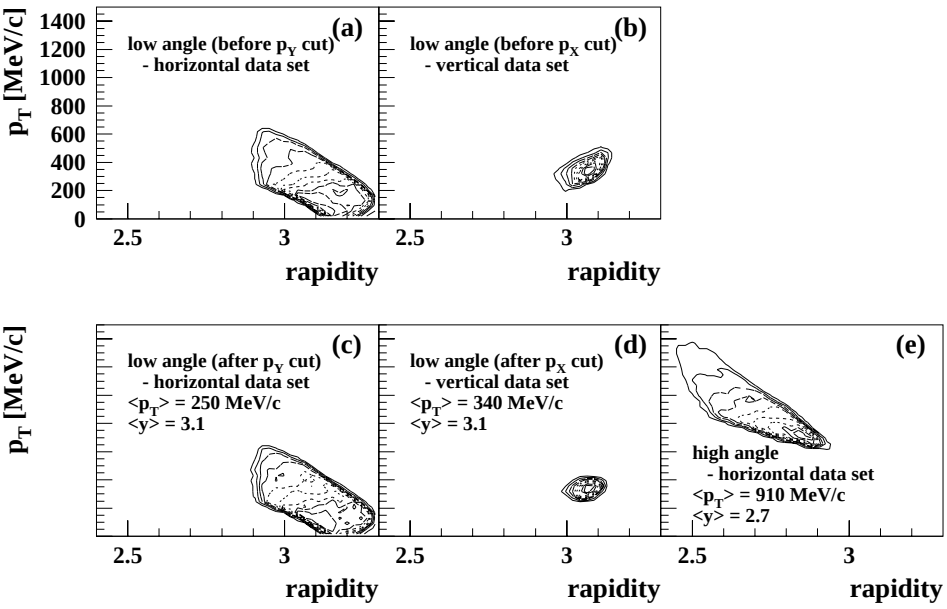

Figure 3.2: Acceptance for configuration of the NA44 spectrometer for three datasets in table. The figures (a–b) show the distribution of the rapidity and transverse momentum with the jaws rescattering of the low angle dataset. The figures (c–d) show the similar distribution, but cut the jaws rescattering. The figure (e) is the distribution of the rapidity and transverse momentum of the high angle dataset. This has originally no jaws. For the detail of the jaws rescattering, see the text.

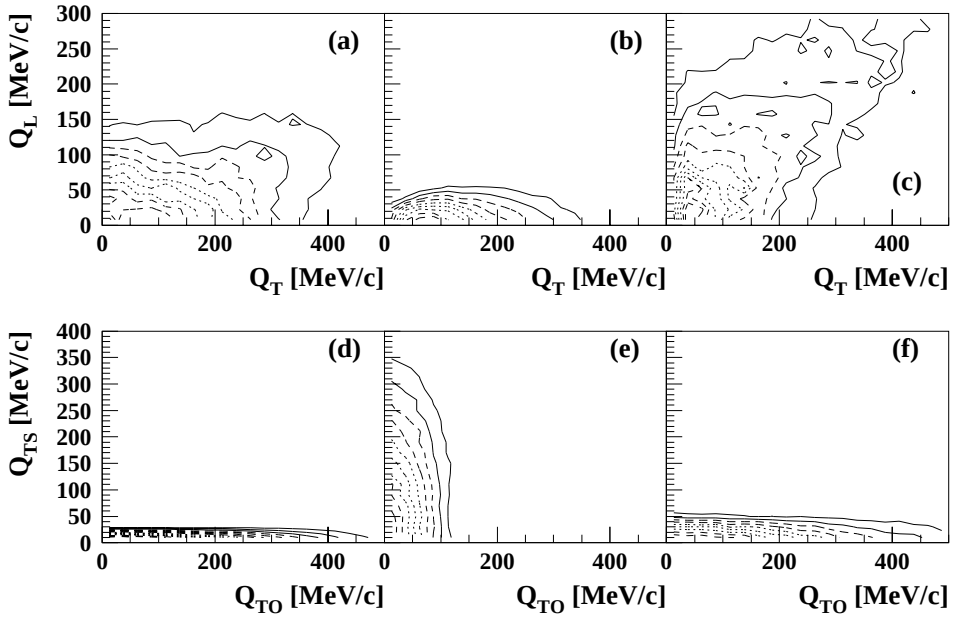

Figure 3.3: Acceptance for the configuration of the NA44 spectrometer for three datasets in table. The figures (a–c) and (d–f) shows the acceptance of the momentum difference in the LCMS for the data of the low angle horizontal setting, the low angle vertical setting, the high angle horizontal setting, respectively.

for the one–dimensional and two–dimensional,[2] but three–dimensional analysis was not done.

The data in these datasets are taken with the two–kaon trigger, which requires for the valid beam (VB), centrality (T0), multiplicity (MUL2) and veto of Cherenkov detectors ($\overline{C1}$, $\overline{C2}$). As the two–kaon triggering rate at the small angle setting is low, data of three–pion trigger ($VB \cap T0 \cap MUL3$) is also mixed simultaneously, at scaled–down factor of 16.

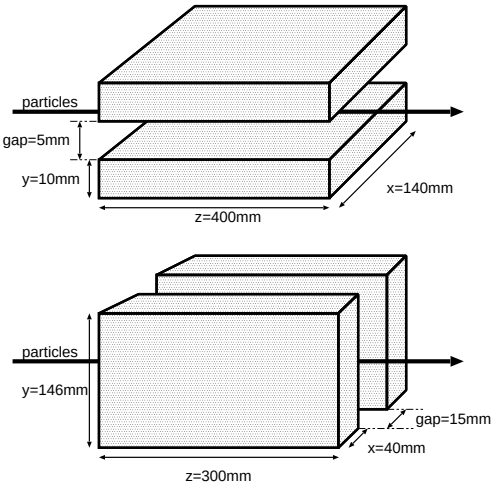

Figure 3.4: Dimension of the horizontal jaws (top) and vertical jaws (bottom). Material of the jaws are tungsten.

Totally, 116 and 103 good runs are taken at the small angle setting with the horizontal and vertical setting during in two weeks. 56×10^3 valid events (for the horizontal setting) and 72×10^3 valid events (for the vertical setting) are accumulated with the two–kaon trigger. At the large angle, a total of 68 good runs which contain approximately 35×10^3 events, are taken over a week.

[2]This analysis performed with Dennis M. Reichhold of Ohio university.[35]

Table 3.1: List of data set used in the KK correlation analysis. In the field of the setting of quadrupole, h and v means the horizontal setting and vertical setting respectively.

dataset	(i)	(ii)	(iii)
data collecting year	1995	1995	1996
collision system (nuclear species)	Pb+Pb	Pb+Pb	Pb+Pb
setting of quadrupole	hori.	vert.	hori.
spectrometer angle	44mr	44mr	131mr
nominal momentum setting [GeV/c]	~ 6.0	~ 6.0	~ 7.5
number of triggered events [$\times 10^3$ events]	26	50	30
number of selected pairs [$\times 10^3$ pairs]	20	20	17
average transverse momentum [GeV/c]	0.25	0.25	0.91
acceptance of rapidity	2.9–3.3	3.0–3.2	2.4–2.9
centrality of collisions	10%		18%

3.4 Centrality

The charged multiplicity is measured by two detectors (T0 and Si). The multiplicity by T0 is used to determine the centrality in this analysis.

T0 consists of two scintillator pads, on the left side and the right side, and the beam line passes through between them. Each pad is read out at the top and the bottom by two PMTs. Lead ions pass through the target produce a large number of low energy electrons (δ–electrons) by knocking them out of the target atoms. Due to the magnetic field of D1, these electrons are mostly swept to one side of the T0 detector. To determine the centrality, the 'δ–clean' side of the T0 detector is used. Since the polarity of the D1 were set to collect positive kaons for this analysis, the δ–clean side is right side viewing in the direction of the beam.

The centrality is defined as a ratio of the number of selected events to the number of all collision events. The event selection includes online (trigger) and offline cuts. To determine the centrality, a special run (VB run) is taken

with only requiring the VB trigger. The centrality (σ_{data}) is calculated as:

$$\sigma_{data} = N_{data} \cdot f_{norm} \cdot \sigma_{\rm VB}/N_{\rm VB}$$

where N_{data} is the number of selected events, $N_{\rm VB}$ is the number of all events in the VB run. f_{norm} is the normalizing factor between the data of VB run and a given dataset. The normalization is done supposing the same distribution of the T0 ADC in large region.

Suppose the VB trigger counts all collision events, the total cross section ($\sigma_{\rm VB}$) is calculated by,

$$\sigma_{\rm VB} = \frac{\lambda_I^{\rm Pb+Pb}}{L \cdot \rho}$$

where L is thickness of target and ρ is density of target. $\lambda_I^{\rm Pb+Pb}$ is an interaction length for a Pb+Pb collision, and it can be deduced from an interaction length for a p+Pb collision ($\lambda_I^{\rm p+Pb}$) using geometrical approximation as,

$$\lambda_I^{\rm Pb+Pb} \sim \lambda_I^{\rm p+Pb} \cdot \frac{A_p^{1/3} + A_{\rm Pb}^{1/3}}{A_{\rm Pb}^{1/3} + A_{\rm Pb}^{1/3}}$$

The centrality in the table 3.1 is deduced for each dataset using the above equations.

3.5 Data selection and pair file

The analysis uses only events which pass several requirements. The selection can be categorized in three types. One is a selection to the global event–by–event information (e.g. CX, T0, C1, C2 and so on). Next is a selection to the track–by–track information (e.g. confidence level of tracking, momentum, mass–squared and so on). After these of selections, pairs of particles are combined, and the 'pairfiles' are made. The last selections is applied to to these pairs in the pairfiles.

3.5.1 Global event requirement

All the event should be clean, which means that only a single beam nucleus must hit the target without accompanying any secondaries from upstream. To require this, a cut of signals of CX1 and CX2 is applied. (See figure 2.4.) To reject the accompanying secondaries, no signal is required to the CX veto counters. The hatched area in the plot (a) and (b) in figure 3.5, are used as the valid data.

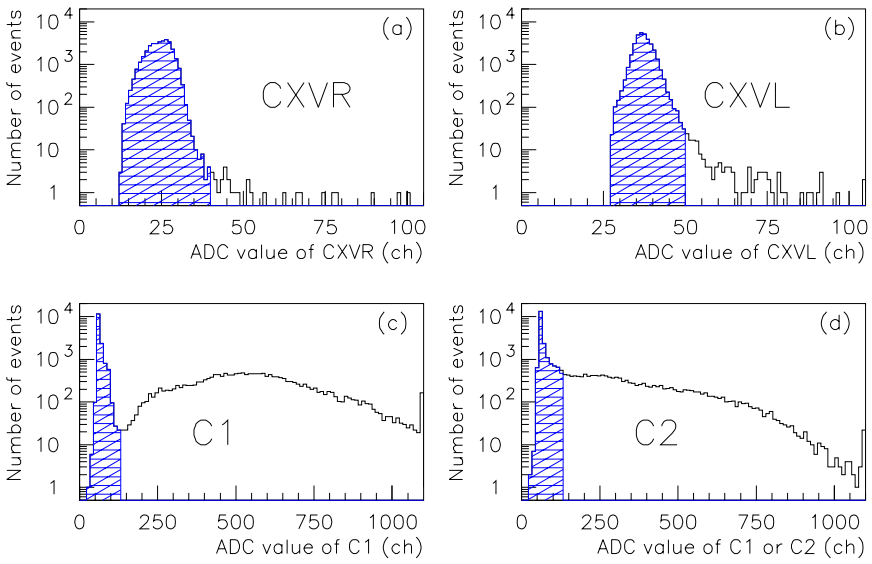

Figure 3.5: The top two figures show ADC distributions of the CX veto counter with right–side PMT (a) and left–side PMT (b). The bottom two figures (c) and (d) show the ADC distribution of C1 and C2 respectively. Hatched areas in all plots shows a region required by the selection.

3.5.2 Particle identification

In the online trigger, the C1 and C2 selection to remove electrons or pions are applied to the data though, another ADC cuts for C1 and C2 are done online, to remove events taken with the three–pion trigger. (See figure 3.5 and 3.6.) The ADC information of C1 and C2 are provided for every event, not for every track. After the selection of C1 and C2, therefore, there is no pion in the events remained. To remove protons, a mass–squared calculated for every track, and kaon tracks are obtained, as shown in the figure 3.7.

The contamination of the pions or protons into the selected kaon tracks are evaluated to be 0.15% and 3.9%, respectively, assuming the distributions of C1 ADC and mass–squared are Gaussian.

3.5.3 Cuts for track quality

Since tracks are found by the fitting, the confidence level for each track can be calculated. Figure 3.1 shows the distribution of confidence level along the horizontal and vertical direction. We discarded the peak around zero.

Slat cuts for the hodoscopes (H2 and H3) remove tracks which hit on the most outer scintillator slats.

During the data taking at the small angle of the spectrometer, the jaws are installed. There are tails of the p_y (p_x) distribution for the data which are caused by rescattering of secondaries at the jaws for the horizontal (vertical) setting. These tracks in the tails (so call jaws tails) which did not come directly from the collision vertex disturbs the correlation. So that these tails are rejected as shown in figure 3.8. Because this cut are most severe function of the particles of interest and make the number of tracks decreases, careful studies for the cut was carried out including studies for the systematic errors.

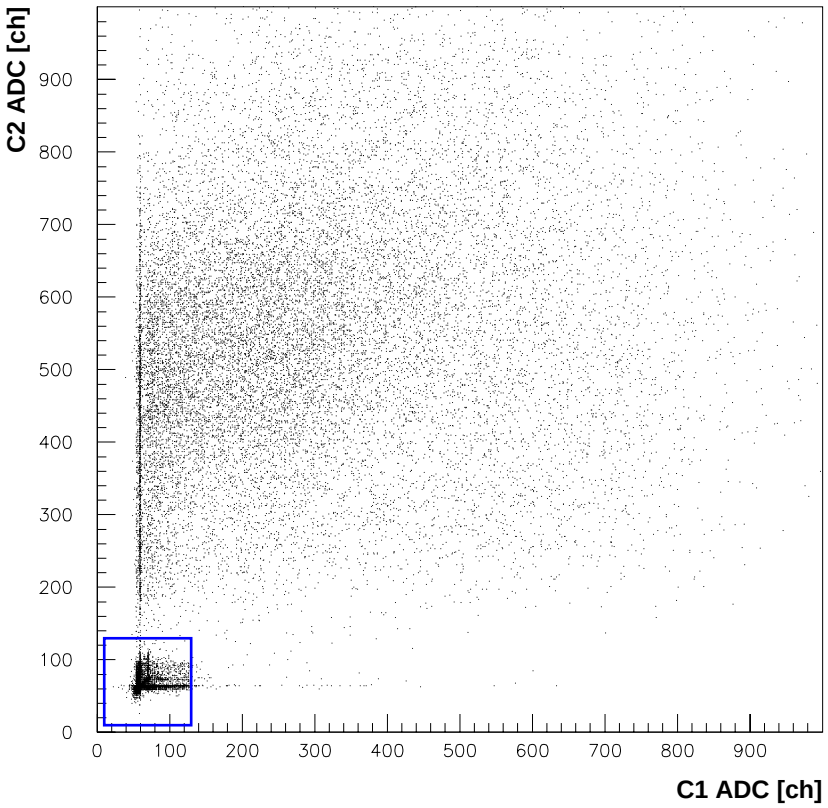

Figure 3.6: A scatter plot of the C1 and C2 ADC. a region in the box (i.e. $\overline{C1} \cap \overline{C2}$), is required. After this requirement, events with only kaons or heavier particles are left.

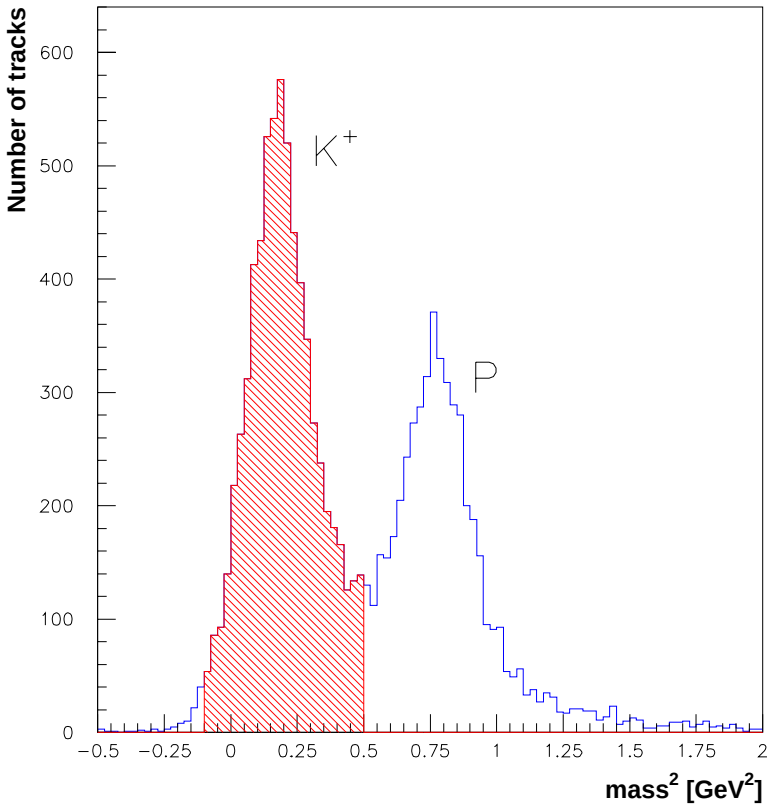

Figure 3.7: A distribution of mass–squared calculated from TOF of H3. The hatched area shows the kaon peak.

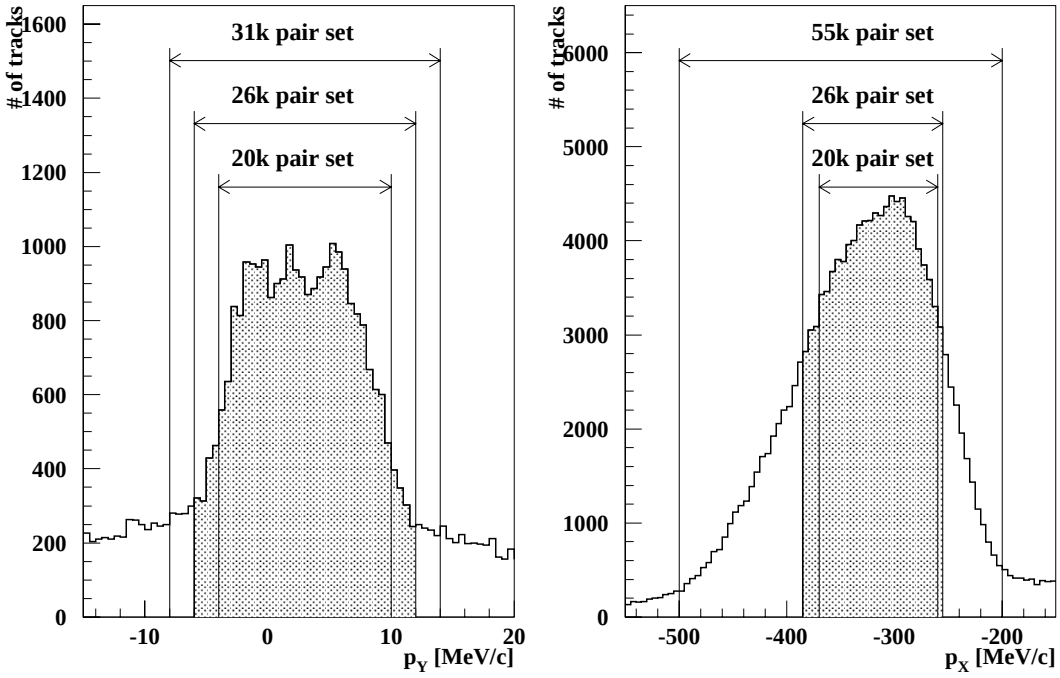

Figure 3.8: The left plot shows a p_y distribution for the horizontal setting with low angle configuration, while the right plot shows a p_x distribution for the vertical setting with low angle configuration. The jaws cuts of three different region are also shown.

3.5.4 Making pair file and cuts for pairs

After event and track selections, the pairfiles are made. This process rejects events which have zero or one kaon–track. If an event has three or more kaon tracks, pairs are made for all pair combination of tracks.

The tracking detectors (PC, SC, H2 and H3) have finite resolutions of hit positions, therefore, it is difficult to separate tracks at a very small distance on a detector. Since PC has the best resolution about 0.5 mm in the tracking detectors, pairs are required to have more than 0.5 mm seperation of a distance between hit positions on the PC.

We found that the pairfiles include more pairs whose tracks traveling parallel each other, than the number of expected by a Monte Carlo simulations. These ghost tracks seem to be produced in the tracking code. To remove the ghost tracks, another cut called "SUMCUT" is applied. The SUMCUT is a cut of summation (dR_{sum}) of a hit distance between two tracks on the PC, H2 and H3. Figure 3.9 shows a ratio of the number of pairs between the real data and simulation as a function of dR_{sum} variable. Pairs which have the dR_{sum} larger than 10 cm are required for valid pairs.

After these cuts, the number of pairs becomes 20×10^3 in both the horizontal and vertical setting for the small angle configuration, while 17×10^3 pairs in the horizontal setting for the large angle configuration.

3.6 Monte Carlo simulation of the spectrometer

The finite acceptance and momentum resolution of the spectrometer introduce distortions of the experimental results. In order to evaluate and correct the distortions, a Monte Carlo (MC) simulation program of the spectrometer

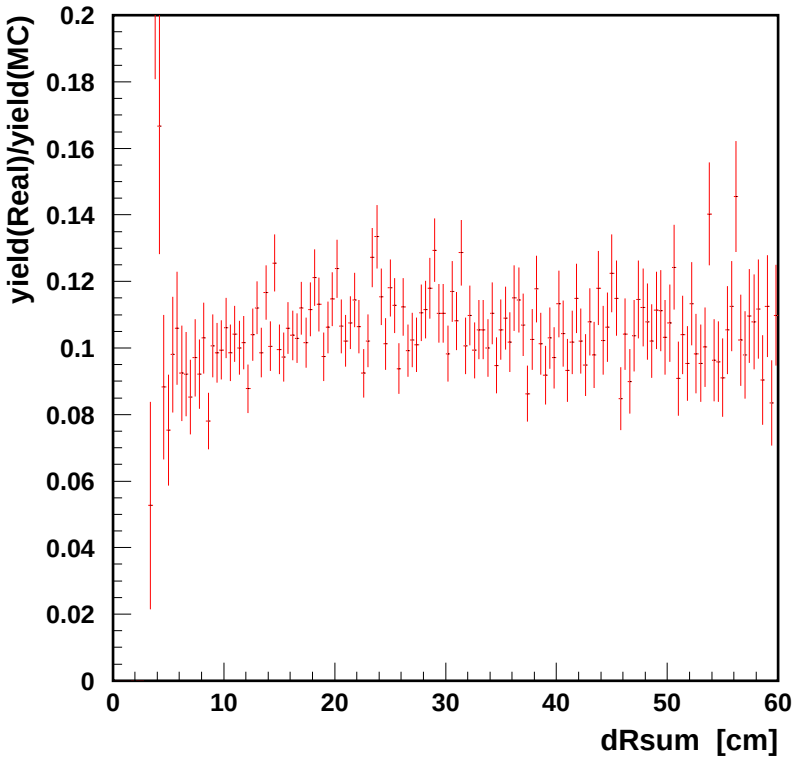

Figure 3.9: Ratios of the number of pairs between the real data and simulation as a function of dR_{sum} parameter.

was developed.

The first step of the simulation is to generate particles with appropriate momentum ($\vec{k}$) and rapidity (y) distributions. The distribution supposed in this analysis is:

$$\frac{1}{m_T^2}\frac{d^2N}{dy\,dm_T} = e^{-m_T/T_{inv}}e^{-(y-y_0)^2/2\sigma^2},$$

where m_T is the transverse mass of the particle, y is the rapidity, T_{inv} is the inverse slope parameter, and σ_y is the width of the rapidity distribution. In this analysis, it is assumed that $T_{inv} = 230\mathrm{MeV}/c$ and $\sigma_y = 1$. Although the validity of this assumption is confirmed from the single particle measurements, however, the uncertainty comes from this assumption was estimated and added into the systematic errors. Several particles can be generated with one spices or a mix or several spices, and two kaons were generated in an event for this analysis.

After the generation of particles, the program simulates tracks of particles in the spectrometer with an appropriate setting, and it simulates hit positions with an appropriate resolution on the tracking detectors. This routine is based on the DECAY TURTLE[34] simulation packages. Using these simulated hit positions, the tracks of particles are reconstructed and simulated momentum is deduced. This routine is the same algorithm as the analysis of the real data. The difference between the initial and reconstructed momentum is estimated as the momentum resolution.

3.7 Correlation function

Using the the selected pairs after the quality cuts, a correlation function is formed. The raw correlation function is defined as:

$$C_2^{raw}(\vec{p_1},\vec{p_2}) = \frac{R(\vec{p_1},\vec{p_2})}{B(\vec{p_1},\vec{p_2})},$$

where the "real distribution" $R(\vec{p_1}, \vec{p_2})$ is the observed distribution of events with particle momenta $\vec{p_1}$ and $\vec{p_2}$, and the "background distribution" $B(\vec{p_1}, \vec{p_2})$ is the distribution of events with $\vec{p_1}$ and $\vec{p_2}$ if there is no quantum interference. The background distribution is experimentally generated from particle pairs from different events of the same data sample. This technique is called as 'event mixing'. The same quality cuts are applied to the mixed (background) pairs as the real data. The number of mixed pairs is ten times larger than the number of real pairs, so that the statistical errors from the background distribution becomes small enough compared with that of the real distribution.

The Coulomb correction, acceptance correction and background corrections for a residual correlation are applied to the raw correlation function. The corrections are expressed by,

$$\begin{aligned} C_2^{corrected}(\vec{p_1}, \vec{p_2}) &= C_2^{raw}(\vec{p_1}, \vec{p_2}) \times K_{CC}(\vec{p_1}, \vec{p_2}) \\ &\quad \times K_{ACC}(\vec{p_1}, \vec{p_2}) \times K_{BG}(\vec{p_1}, \vec{p_2}), \end{aligned}$$

where $K_{CC}(\vec{p_1}, \vec{p_2})$ is the factor for the Coulomb correction, $K_{ACC}(\vec{p_1}, \vec{p_2})$ is for the acceptance correction and $K_{BG}(\vec{p_1}, \vec{p_2})$ is for the background correction. These factors are not only a function of the momenta ($\vec{p_1}$ and $\vec{p_2}$), but also on the shape of correlation function of interest. Therefore an iterative procedure is necessary. The parameterized shape of the correlation function from the previous iteration is used in the calculation of each correction and then the correlation function is formed. The results of parameterization are typically converged with five iterations. In this analysis, twelve iterations were done.

3.7.1 Residual correction

The background distribution is generated by the event mixing method. It was assumed that there are no Bose–Einstein correlations between the particles.

Some residual correlations remain in the mixed–pair, and the strength of these correlations is inversely proportional to the size of measurement acceptance.[36, 37] Since the acceptance of the NA44 spectrometer is rather small, the residual correlation can be significant and needs to be removed for the raw correlation function.

3.7.2 Coulomb correction

There is a Coulomb repulsion force between two tracks. This effect decreases the amplitude of the correlation function at small momentum difference. For a large source, the Coulomb wave function integration technique becomes more accurate than the Gamow correction which assumes a point–like source.[13] The actual source should have a finite size, as it is produced by a nuclear collision. The effect of the finite source size of the kaon pairs is bigger than one of pion pairs, because kaons stay longer time around the source than pions with similar momentum. Since the Coulomb wave function integration method integrates over the finite source size, it is necessary to know the source size for the calculation of the Coulomb correction factor. The calculation is done iteratively, and the source size is taken from the parameterized function of a previous iteration.

3.7.3 Acceptance Correction

The finite acceptance of the spectrometer distorts the correlation function. The signals of the particle interferometry exist in a region of the small momentum difference between a pair particle, however, the signal is distorted

due to the finite momentum resolution and the two–track resolution of the spectrometer. This distortion is corrected by the MC simulation.

Using the MC simulation, two correlation functions are calculated. One is the ideal correlation function ($C_2^{ideal}(\vec{p_1}', \vec{p_2}')$) which is formed using inputted momentum (or momentum measured by a perfect detector) of pairs. Another is the reconstructed correlation function ($C_2^{recon.}(\vec{p_1}, \vec{p_2})$) which is formed using momentum reconstructed through the detector simulation. The uncertainty of momentum measurement is estimated by the difference of the reconstructed momentum from the inputted momentum in the simulation. Note that the $C_2^{ideal}(\vec{p_1}', \vec{p_2}')$ and $C_2^{recon.}(\vec{p_1}, \vec{p_2})$ include also the effect of the Bose–Einstein correlation and the distortion by the final state Coulomb interaction. Therefore the acceptance correction also depends on the shape the correlation function. This requires the iterative analysis as same as the Coulomb correction. Then the factor of the acceptance correction ($K_{ACC}(\vec{p_1}, \vec{p_2})$) can be calculated as:

$$K_{ACC}(\vec{p_1}, \vec{p_2}) = \frac{C_2^{ideal}(\vec{p_1}', \vec{p_2}')}{C_2^{recon.}(\vec{p_1}, \vec{p_2})}.$$

Using this factor, the correlation functions are corrected.

3.8 Systematic error estimation

In the analysis procedure, the following parameters are arbitrarily decided. To evaluate uncertainties to the correlation functions form these parameters the correlation functions are re-calculated using parameters which are artificially changed from the nominal values. These parameters are classified in three types, that are parameters using in the MC, the data selection, and for fitting procedure. They are itemized as the followings:

(The symbol name of the parameter is also shown in parentheses.)

1. Parameters used in the Monte Carlo simulation

   There are many parameters in the Monte Carlo, but most parameters have fixed values determined by the geometry of real detector or same of them do not effect to the analysis result. The followings are included in the systematic errors.

   (a) The target thickness affects to the momentum resolutions due to the multiple scattering. Measured thickness of the target is 0.313 cm. For the evaluation of the systematic error, the thickness is changed for $\pm 10\%$, but the results of the source parameters are not changed beyond in the statistical errors. (`TARGTTH`)

   (b) The particles in the MC have an exponential distribution of the transverse momentum. The inverse slope parameter of this function could change the results. Nominally, the value of 230 MeV are used. The $\pm 5\%$ from this value are studied for the systematic error evaluation. The inverse slope is decided from the analysis of the transverse momentum distribution. The systematic errors with the inverse slope parameter are changed only in the statistical errors. (`SLPTPAR2`)

2. Parameters for the data selection

   The criteria for the data selection might be arbitrary, but the final results should not depend on the parameters of the arbitrary criteria. This was confirmed for the following items. For the detail of the data selection, please see the section 3.5.

   (c) To remove ghost tracks, tracks with similar hit positions near

to each other are discarded by the "SUMCUT" parameter, as described in the sub–section 3.5.4. (`SUMCUT`)

(d) A distribution of distance between hit positions of a pair on the pad chamber does not represent a distribution of the real data around the small distance. This is caused by the ghost tracks. We remove pairs which have hit distance on the pad chamber is smaller than 0.5 cm in the normal case. No cut and cut with 1.0 cm are also tried. The fitting results are nearly changed. (`PAD1CUT`)

(e) As each strip chamber is consisted of four layers (x and y layers each in the SC1 and the SC2), each track has four hits in normal. However, some layers have dead channels, so the reconstruction efficiency of the tracks becomes low relatively if it requires all four layers have a hit. Tracks are usually required to have three hits out of a layers in the track reconstruction. Therefore a pair has 6 or more hits of the strip chambers in the normal cases. To estimate the systematic errors, I studied the final results requiring the minimum hit number of the strip chambers to be 7 and 8. (`NSC_CUT`)

(f) Cut width of jaws tails for p_y of horizontal data and p_x of vertical data. (`JAWSCUT`)

As the jaws cuts are serious to the data sample, the results could has large systematic errors.

3. Choice of analytical methods and parameters in the fitting procedure

(g) The correlation function is filled into a histogram for the analysis. The bin width of the correlation function is arbitrarily decided, and it is normally 10 MeV/c. For the estimation of the systematic

errors, 12 and 15 MeV/c are also studied. The systematic errors are relatively large changing the bin width.(BINSIZE)

(h) The number of contents in each bin of the histogram of the correlation function are required minimum number for the fitting to deduce the source parameters. The nominal value is 10, and I tried the cases of 5 and 20 for the evaluation of the systematic errors, which was so small in result. (MINCNT)

(i) The first bin of the correlation functions has very low statistics but most effects to the source parameters. Normally the first bin is included for the fitting, but I studied a case excluding the first bin in the fitting. (Q_ST)

(j) Two–lambda fitting is also studied. In the three–dimensional analysis, datasets of horizontal and vertical settings are used. On the fittings to both histogram of these datasets, a unique lambda parameter are used in the usual case. For the certification, two different parameters of lambda are used for the fitting. Difference of two lambda are a little bit large, but it is is the statistics.(FIT_MD)

For each item, the systematic errors are evaluated. The results of the evaluation are listed in table 3.2. A part of them (JAWSCUT, MINCNT, TARGTTH, SUM_CUT, BINSIZE and SLPTPAR2) are used to deduce an integrated systematic errors, because the other items have trivial difference with good reasons. Finally, the systematic errors of fitting parameters are less than 10% for three–dimensional analysis, and 20%–30% for one or two–dimensional analysis. They are comparable to the statistical errors. The exact value of the systematic errors will be presented in the chapter 4.

Table 3.2: Systematic errors on extracted source parameters for each source of errors. Some sources of systematic errors indicated by an asterisk ($*$) are integrated and listed. Statistical errors are also listed for reference.

source of systematic error	λ	R_{TS}	R_{TO}	R_L
(a) TARGTTH*	1.0%	1.7%	0.6%	0.4%
(b) SLPTPAR2*	0.1%	2.2%	1.2%	0.5%
(c) SUMCUT*	6.1%	6.3%	5.6%	5.5%
(d) PAD1CUT	0.8%	0.8%	0.8%	0.7%
(e) NSC_CUT	3.0%	14.8%	23.4%	7.9%
(f) JAWSCUT*	2.4%	0.9%	1.1%	2.3%
(g) BINSIZE*	4.5%	3.6%	4.6%	0.4%
(h) MINCNT*	0.2%	0.4%	0.2%	0.2%
(i) Q_ST	22.2%	12.1%	16.1%	14.2%
(j) FIT_MD	3.0%	4.6%	4.4%	4.4%
integrated systematic errors	8.0%	7.8%	7.5%	6.0%
statistical errors	6.7%	7.0%	6.2%	7.5%

Chapter 4

Results

In this chapter, the correlation functions of two positive kaons in the central Pb+Pb collisions are presented. There are one–dimensional, two–dimensional and three–dimensional correlation functions from the data at the lower transverse momentum (taken with the small angle setting), and the one–dimensional and two–dimensional ones from the data at the higher transverse momentum (taken with the large angle setting). The results of Gaussian parameterization are also presented.

4.1 One–dimensional correlation functions

As described in the chapter 1.3, the fitting equation used in the one–dimensional correlation function is:

$$C_2(Q_{inv}) = A(1 + \lambda\ exp(-Q_{inv}^2 R_{inv}^2))$$

where A is a normalizing parameter and Q_{inv} is the Lorentz invariant variable of four momentum difference between a pair. The one–dimensional fit to the K^+K^+ correlation function is shown in figure 4.1 using the data for the small and the large angle configurations of the spectrometer. Although we have two datasets; horizontal and vertical settings for the small angle configuration, I

used only the horizontal data for the one–dimensional and two–dimensional analyses because of its better resolution. All corrections: the background correction, the acceptance correction with the Monte Carlo simulation, the final state Coulomb interaction with the Coulomb wave function integration technique, have been applied to this function. The error bars in figure 4.1 show the statistical ones, as will be shown in all plots of the correlation functions. Around the small Q_{inv}, bins of the correlation functions has low statistics and hence have large error bars. Especially, for the correlation function of the large angle setting, the first bin (0–10 MeV/c) is empty. Therefore, the first and the second bins for the large angle setting were excluded from for the fitting.

The parameters from Gaussian fitting for the small angle dataset ($\langle p_T \rangle = 250\mathrm{MeV}/c$) and the large angle dataset ($\langle p_T \rangle = 910\mathrm{MeV}/c$) are listed in table 4.1. The transverse momentum and the centrality are also shown. The χ^2 and the degree of freedom (d.o.f.) for the fitting are also included.

The χ^2/d.o.f is about one, which implies that the assumption of a Gaussian form is reasonable. The R_{inv} at the lower transverse momentum is larger than that at the higher transverse momentum. It indicates that the source size depends on the transverse momentum. More discuss about the dependence of the transverse momentum will be described later.

4.2 Two dimensional correlation functions

Because it is hard to assume the source can be well expressed only by one–dimensional parameter (Q_{inv}), two dimensional correlation function is extracted and the distribution is parameterized with Q_T and Q_L. As described in the next section, a three–dimensional fit is more useful than the two–dimensional fit. Because we have no vertical data and the statistics is lim-

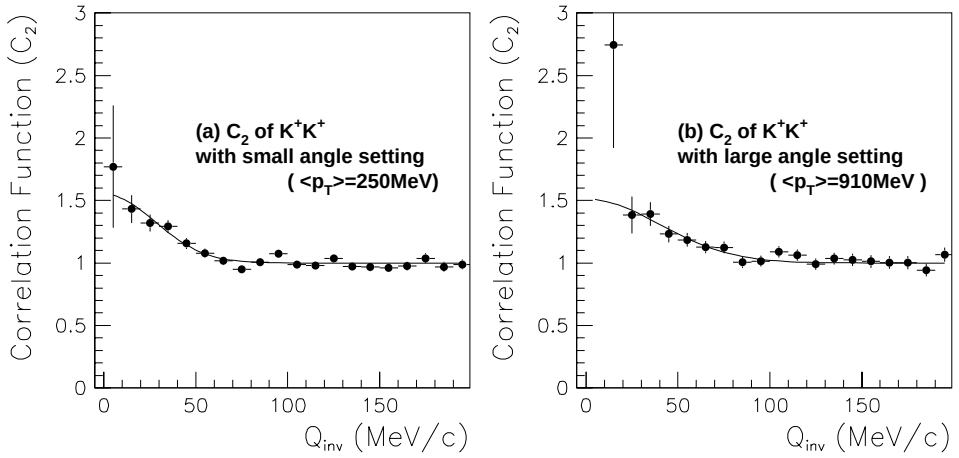

Figure 4.1: The one–dimensional correlation function of kaon pair in Q_{inv} for the small angle setting (left) and the large angle setting (right), after corrections. The bin width is 10 MeV/c. The error bars show statistical errors only. The solid line is the fit function.

Table 4.1: Fit results of Gaussian parameterizations of the KK correlation function at small angle dataset ($\langle p_T \rangle = 250$MeV/$c$) and large angle dataset ($\langle p_T \rangle = 910$MeV/$c$) for one–dimensional analysis. The errors are statistical and systematic.

setting	small angle KK	large angle KK
$\langle p_T \rangle$	0.25 GeV/c	0.91 GeV/c
centrality	10%	18%
λ	$0.55 \pm 0.09 \pm 0.17$	$0.47 \pm 0.12 \pm 0.08$
R_{inv} [fm]	$5.09 \pm 0.44 \pm 0.37$	$3.28 \pm 0.62 \pm 0.75$
χ^2/d.o.f.	32/37	21/26

ited for the horizontal data at the large angle configuration, the correlation functions for the large angle dataset have been done only in two-dimensional axes. For the comparison, a correlation function of the small angle dataset is also extracted. With the Bertsch–Pratt parameterization in the LCMS reference frame, the equation used for the two–dimensional fit is

$$C_2(Q_T, Q_L) = A(1 + \lambda exp(-Q_T^2 R_T^2 - Q_L^2 R_L^2)),$$

where A is a normalization parameter. In figure 4.2, projections of the correlation functions to each Q_T and Q_L are shown for the data at the small angle setting (top figures; $\langle p_T \rangle$ = 250 MeV/c) and large angle settings (bottom figures; $\langle p_T \rangle$ = 910 MeV/c) after corrections. The bin width is 10 MeV/c for the small angle dataset, while 20 MeV/c for the large angle dataset due to its lower statistics. The solid line represents a projection of the fit function.

Table 4.2 shows the parameters extracted from the fits to the two–dimensional correlation functions, along with the transverse momentum and the centrality. As the large angle data sample has lower statistics, the degree of freedoms (d.o.f.) is smaller than that of the small angle data sample. As similar as the result of one–dimensional fits, the χ^2/d.o.f. is close to one, which shows the validity of the Gaussian parameterization. The source size parameters (both of R_T and R_L) have the transverse momentum dependence as is seen in a case of one–dimensional analysis.

4.3 Three dimensional correlation functions

The three dimensional analysis can provide the significantly more important information than one– or two–dimensional analysis. The three–dimensional analysis in the NA44 experiment, however, requires a pair of data of the horizontal setting and the vertical settings, due to the limit of detection

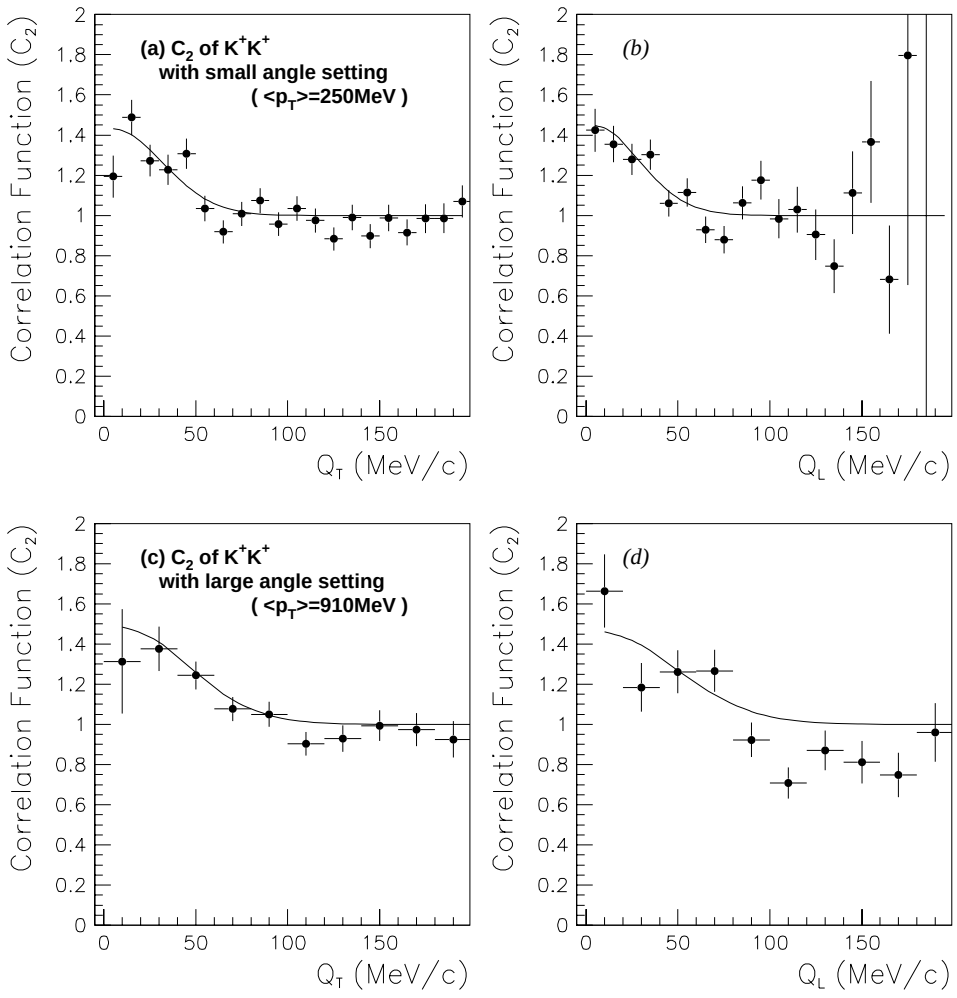

Figure 4.2: The projections of the two dimensional correlation functions of kaon pair at $\langle p_T \rangle = 250$ MeV/c (top) and $\langle p_T \rangle = 910$ MeV/c (bottom). The error bars show statistical errors only. The solid line is the fit function.

Table 4.2: Fit results of Gaussian parameterizations of the KK correlation function at small angle dataset ($\langle p_T \rangle = 250$ MeV/c) and large angle dataset ($\langle p_T \rangle = 910$ MeV/c) for two–dimensional analysis. The errors are statistical and systematic.

setting	low angle KK	high angle KK
$\langle p_T \rangle$	0.25 GeV/c	0.91 GeV/c
centrality	10%	18%
λ	$0.57 \pm 0.09 \pm 0.14$	$0.61 \pm 0.20 \pm 0.16$
R_T [fm]	$4.75 \pm 0.49 \pm 0.57$	$3.59 \pm 0.67 \pm 0.97$
R_L [fm]	$5.17 \pm 0.61 \pm 0.45$	$3.20 \pm 0.54 \pm 0.45$
χ^2/d.o.f.	432/448	117/107

acceptance of the NA44 spectrometer. All data presented have been analyzed in LCMS reference frame and fit using the Bertsch–Pratt parameterization,

$$C_2(Q_{TO}, Q_{TS}, Q_L) = A\{1 + \lambda exp(-Q_{TO}^2 R_{TO}^2 - Q_{TS}^2 R_{TS}^2 - Q_L^2 R_L^2)\},$$

where A is a normalization parameter. Note that the horizontal and vertical settings are allowed to have different normalization parameters during the fitting process, therefore there are six fitting parameters in the three–dimensional analysis.

Projections of the three–dimensional correlation function are shown in figure 4.3. These projections extend over the lowest 40 MeV/c in the other directions of the momentum difference. The open and solid points indicate the correlation function for the horizontal setting and the vertical settings, respectively. The curves indicate the fitted Gauss function.

Table 4.3 lists the Gaussian fitted parameters of the three dimensional correlation functions in the small angle setting. The transverse momentum and the centrality are also shown in the table. For the reference of the further discussion, the results of the pion interferometry[38] are also listed. Even though the pion data has larger statistics, the d.o.f. of the pion correlation

functions is smaller than that of the kaon correlation function, because a minimum entry in a bin is required to be 100 or larger for the fitting of the pion correlation functions.

Table 4.3: Fit results of Gaussian parameterizations of the KK correlation function at low and high p_T dataset. The errors are statistical and systematic.

setting	small angle KK	small angle $\pi\pi$	large angle $\pi\pi$
$\langle p_T \rangle$	0.25 GeV/c	0.17 GeV/c	0.48 GeV/c
centrality	10%	15%	18%
λ	$0.84 \pm 0.06 \pm 0.07$	0.569 ± 0.035	0.679 ± 0.034
R_L [fm]	$4.36 \pm 0.33 \pm 0.32$	6.58 ± 0.48	3.96 ± 0.23
R_{TS} [fm]	$4.04 \pm 0.28 \pm 0.32$	5.87 ± 0.58	4.39 ± 0.31
R_{TO} [fm]	$4.12 \pm 0.26 \pm 0.31$	5.50 ± 0.26	4.39 ± 0.18
χ^2/d.o.f.	5139/2978	1423/1720	1125/1574

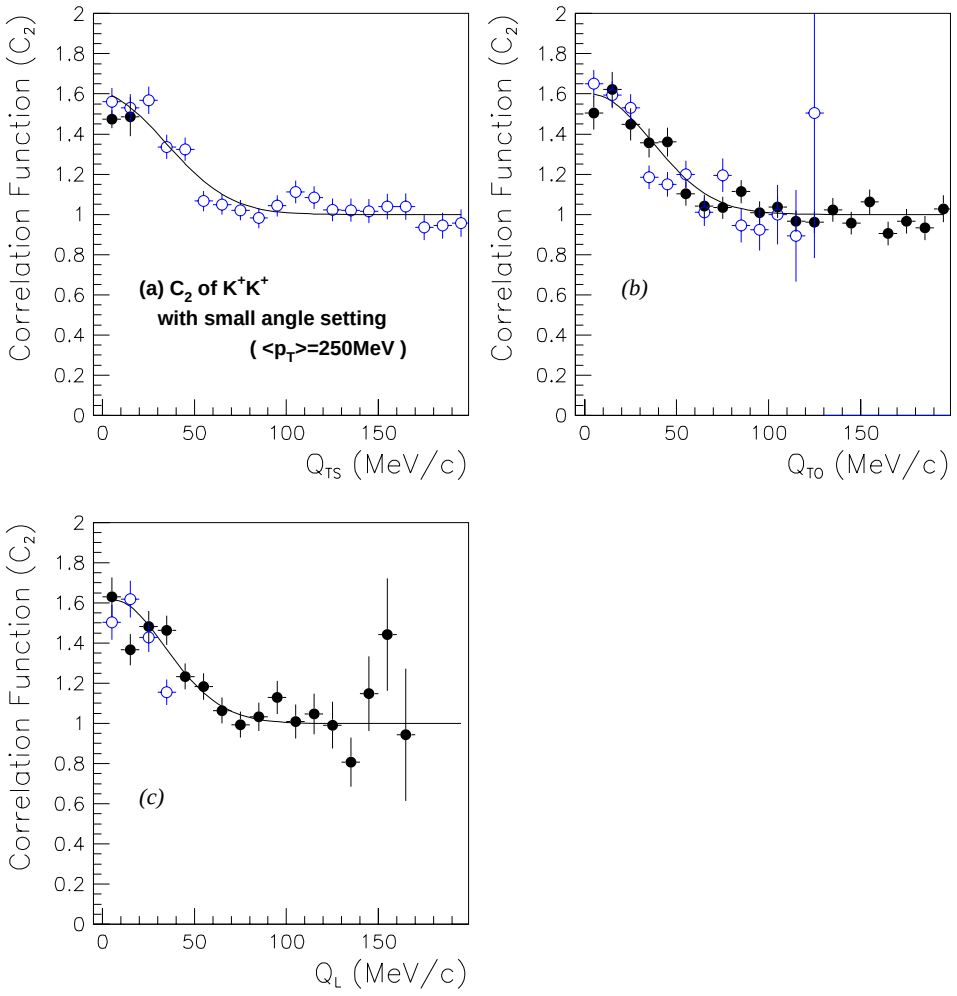

Figure 4.3: The projections of the three dimensional correlation functions of kaon pair at $\langle p_T \rangle$= 250 MeV/c. The coordinate system is the LCMS reference. The error bars show statistical errors only. The solid line is the fit function.

Chapter 5

Discussion

5.1 Radius of beam ions

The spatial extent of a cold nucleus is known well as the Woods–Saxon distribution and can be scaled by the mass number A, i.e. $r_s \sim r_0 A^{1/3}$ and almost have a hard sphere with a constant density inside, where $r_0 = 1.21$ fm. To compare the radius parameters measured with the correlation function to such a geometrical size, it is necessary to convert the radius of the hard sphere (r_s) to the R.M.S. radius ($r_{rms,3d}$) which is related by a factor $\sqrt{3/5}$:

$$r^2_{rms,3d} = \frac{\int_0^{r_s} r^2 d^3r}{\int_0^{r_s} d^3r} = \frac{3}{5} r_s^2$$

On the other hand, the radius parameter from the correlation function is the one–dimensional R.M.S. radius ($r_{rms,1d}$), and thus it is smaller by a factor $\sqrt{3}$ than the three–dimensional R.M.S. radius ($r_{rms,3d}$). I.e.:

$$r_{rms,1d} = \frac{1}{\sqrt{3}} r_{rms,3d} = \frac{1}{\sqrt{5}} r_s$$

The nuclear radius of a lead (Pb) thus becomes $r_s^{Pb} \sim 7.2$ fm and $r_{rms,1d}^{Pb} \sim 3.2$ fm. The radius parameters from the correlation functions are compared with this value in the next section.

5.2 Comparison to the other experimental results

Pion and kaon interferometry measurements were performed by the NA44 collaboration for the system S+Pb at 200 GeV per nucleon and p+Pb at 450 GeV. [39, 40, 41, 42]

The figure 5.1 shows the fitted results (circles for R_{TS}, squares for R_{TO}, triangles for R_L) from the three–dimensional correlation functions of $\pi^+\pi^+$ (open) and K^+K^+ (solid) for the p+Pb, S+Pb and Pb+Pb collisions. Note that in the p+Pb and S+Pb correlation analysis, the Gamow correction for Coulomb final state interaction was used instead of the Coulomb wave function integration technique presently applied. The smaller source size indicates that the Gamow correction is enough for the very good approximation of the Coulomb wave calculation. The horizontal axis shows the radius of projectile nuclei (r_s in the previous section) and the line shows a function of the one–dimensional R.M.S. radius: $r_{rms,1d} = \frac{1}{\sqrt{5}}\, r_s$.

At the first look, the source parameters for both of kaons and pions becomes bigger with increasing the size of projectile nucleus. The source size parameters are always larger than the $r_{rms,1d}$ by 0.5–1.0 fm. Especially, the R_{TS}, which means the transverse radius, shows this tendency clearly. The pion source size is always bigger than the kaon source size. These tendencies are accountable by the model of the collective flow. See the section 5.3.

In the comparison of the directed source size parameters, the R_L is the biggest in every system. The R_{TO} is bigger than the R_{TS} for kaons, while an inverse relation are made up for pions. This difference could be explained with some difference of the duration time. See the section 5.4 about the discussion of the duration time.

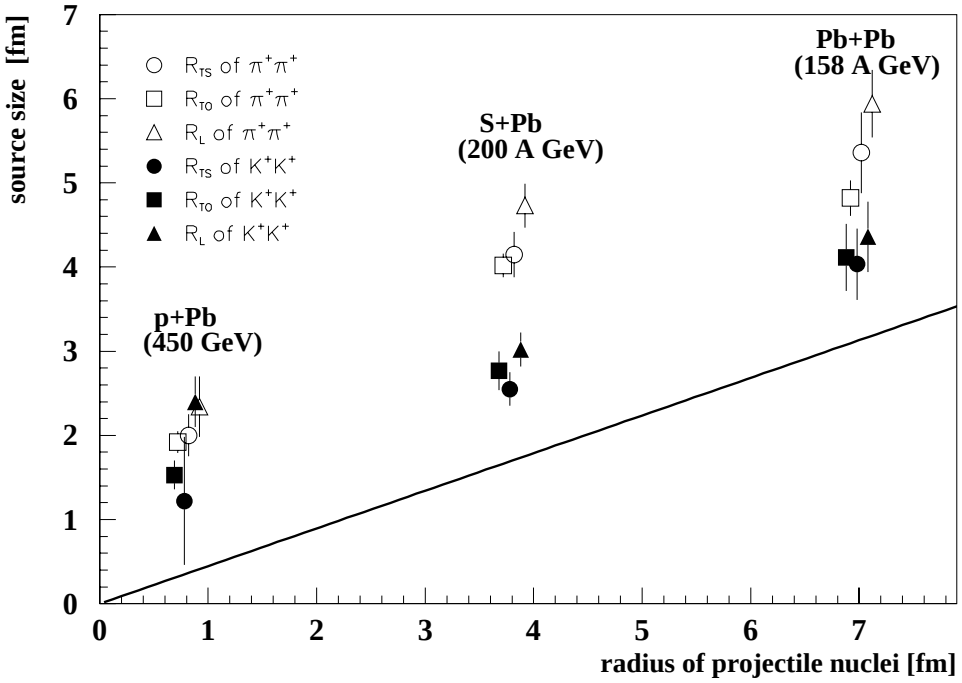

Figure 5.1: The fitted results (circles for R_{TS}, squares for R_{TO}, triangles for R_L) from the three–dimensional correlation functions of $\pi\pi$ (open) and KK (solid) for the p+Pb, S+Pb and Pb+Pb collisions. The horizontal axis shows the radius of the projectile nuclei (r_s in the previous section) and the line shows the one–dimensional R.M.S. radius.

5.3 Transverse mass dependence

The pion interferometry in S + Pb collisions [41, 27] showed the dependence of radius parameters on transverse mass (m_T), which is a quadratic sum of the transverse momentum and the mass, i.e. $m_T = \sqrt{p_T^2 + m^2}$. Simple hydrodynamical models predict the HBT radius parameters would scale to $1/\sqrt{m_T}$ for particles boosted by the hydrodynamical motions.[46, 44] The collective expansion leads to strong momentum–position correlations in both longitudinal and transverse directions. The experimental radius parameters are interpreted as a convoluted value of a geometrical size R_{geom} and a local length of thermalization R_{therm}.

To study the m_T dependence of the source size in Pb + Pb collisions, the experimental longitudinal and transverse radius parameters are plotted in figure 5.2. The radius parameters are deduced from the three–dimensional analysis of pion interferometry[38], and the results of this analysis of kaon interferometry.[43] To confirm the tendency of the m_T dependence, the results of R_T and R_L from the two–dimensional analysis of high p_T data are also plotted. They seem to be on the trend. The solid curves on the both plots show the fit function with a single scaling curve, $R = A/\sqrt{m_T}$. The fitting parameter $A = 3.0 \pm 0.2\mathrm{fmGeV}^{1/2}/c$ in both cases. (The dashed line shows the fit function to only the pion results in the reference [38]. The trends seem to be consistent.

According to a simple hydro–dynamical model by Makhlin and Sinyukov[46], the longitudinal radius parameter R_L depends on the transverse mass m_T with $R_L = \tau\sqrt{T/m_T}$, where T is the local temperature of a source at the freeze–out time τ. That is $A = \tau \cdot \sqrt{T}$. T can be a function of position, but we assume a homogeneous temperature at about 100–140 MeV. Then, the

freeze–out time τ is deduced to be 7–10 fm/c.

We know another dependence of the source size parameters. It is a so–called centrality dependence.[47, 48] So we should note how it causes the difference between the pion and kaon source size rather than the transverse mass dependence. The centrality of the pion and kaon interferometry is shown in the table 4.3. The centrality of the pion data sample is smaller. According the NA44 former analysis [48], the difference of the centrality hardly affects the dependency of the transverse mass.

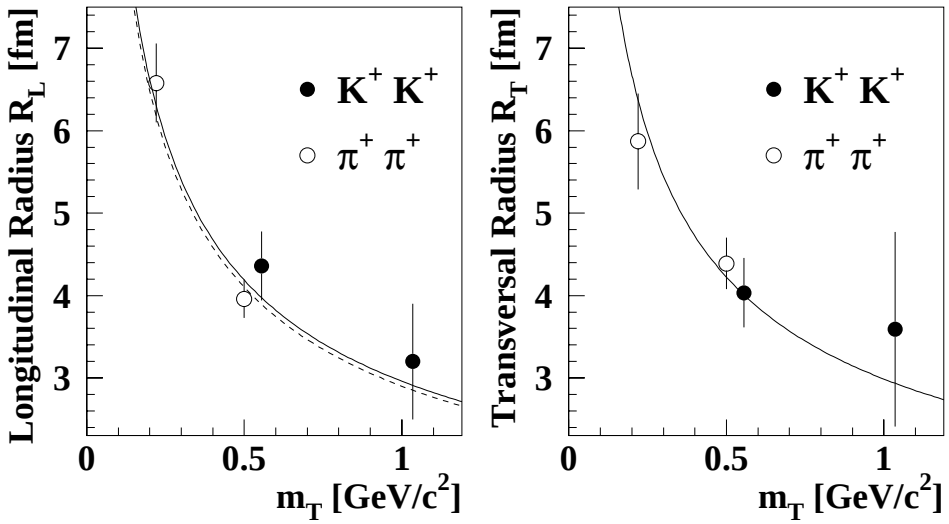

Figure 5.2: The longitudinal and transversal source–size parameters of K^+K^+ at $p_T \approx 0.25$ and 0.91 GeV/c (solid circles), compared with those of pions (open circles). The dashed curve shows a fit to $R = A/\sqrt{m_T}$ for pions, while the solid curve is the fit to the pion and kaon data points in each plot.[38, 43]

5.4 Duration time

From the three–dimensional analysis, the duration time can be deduced as a quadratic difference of the radius parameters between outward (R_{TO}) and sideward (R_{TS}):

$$\Delta\tau = \frac{1}{\beta_T}\sqrt{R_{TO}^2 - R_{TS}^2}$$

where β_T is the transverse velocity of the pair as described in the section 1.3.3.

In a first order phase transition from the quark–gluon plasma, it is expected that there will be a long duration of particle emission. Thus the duration time calculated above function would be a signature of the quark–gluon plasma.

For the $\pi^+\pi^+$ measurement, R_{TO} is similar to the R_{TS}, even a little bit less than R_{TS}. The figure 5.3 shows the quadratic difference, i.e. $R_{TO}^2 - R_{TS}^2$, for the each collisions system. It is easy to find that the duration time is consistent to be zero for each case. This implies there is no long duration time observed in these measurements.

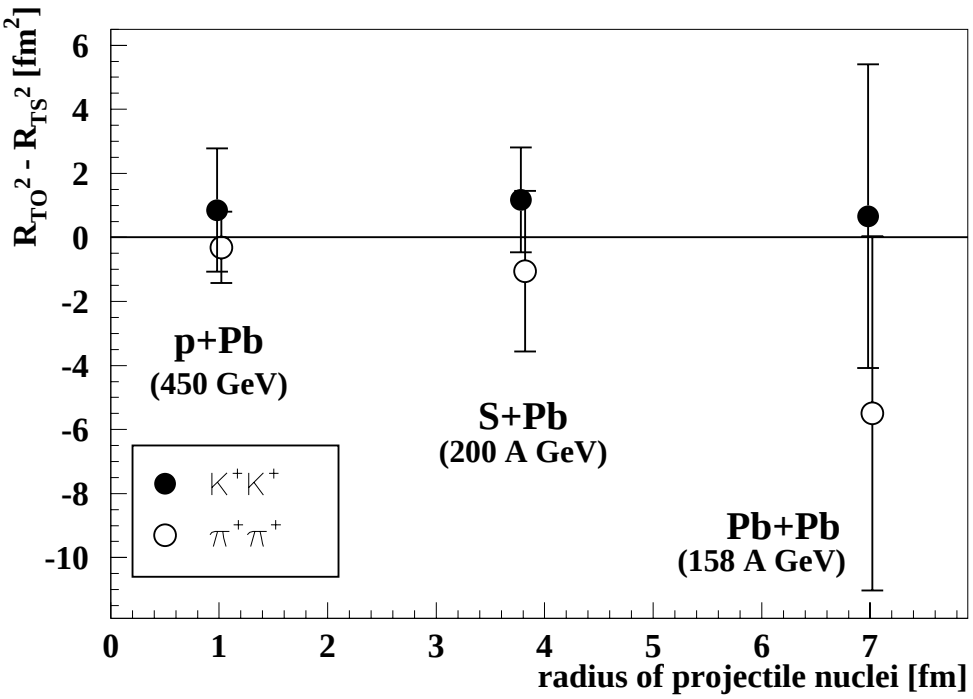

Figure 5.3: Quadratic difference of the R_{TO} and R_{TS} from the results of pion and kaon interferometry for the NA44 experiment.

Chapter 6

Conclusion

Two–kaon correlation function is measured in the central Pb + Pb collisions at 158 A GeV/c by using the NA44 spectrometer at CERN–SPS. The source size parameters are extracted from the correlation functions. The longitudinal, sideward and outward radius parameters (R_L, R_{TS} and R_{TO}) in the three–dimensional analysis are found to be $4.36 \pm 0.33 \pm 0.32$ fm, $4.04 \pm 0.28 \pm 0.32$ fm and $4.12 \pm 0.26 \pm 0.31$ fm, respectively at the averaged transverse momentum $< p_T > \sim 250$ MeV. We also measured the longitudinal and transverse radius parameters (R_L and R_T), being $3.20 \pm 0.54 \pm 0.45$ fm and $3.59 \pm 0.67 \pm 0.97$ fm, respectively in the two–dimensional anlaysis at a higher transverse momentum $< p_T > \sim 910$ MeV.

The results of pion and kaon interferometry with three different projectiles (proton, sulphur and lead ion) are compared. The radius parameters of kaon sources are bigger than the projectile radii by around 1fm. Moreover, those of pion sources are bigger by about 1 fm than that of kaons. The difference of the radii between pions and kaons can be explained by a scaling feature to the transverse mass. This tendency is consistent with simple hydro-dynamical models. According to the simplest model, we could deduce the freeze–out time (τ) for the central Pb + Pb collisions to be 7–10 fm/c. Their results

are consistent with the results by the NA49 and the WA98 experiments.

The duration time ($\Delta\tau$) at a freeze–out in the collision is studied from the measurement at the lower averaged transverse momentum ($\sim$ 250 MeV). We found it is consistent with zero, no unusual long duration time which was expected to be one of a signal of the first order phase transition from the quark–gluon plasma, was observed.

Acknowledgements

Many people contributed to the analysis for this thesis, directly and indirectly. To all of them, I wish to express my sincere gratitude.

First of all, I thank all members of the NA44 collaboration. The data used in my thesis is taken by the NA44 collaboration. Prof. Hans Bøggild (NBI), Prof. Barbara V. Jacak (SUNY), and Prof. Bengt Lörstad (Lund univ.) gave me constructive suggestions for the analysis of this thesis. Prof. Jan Pluta (Nantes) and Prof. Michael Murray (Texas A&M univ.), their deep consideration for the results of the kaon correlation contribute my work with another viewpoint to them. Prof. John P. Sullivan (LANL) and Dr. David H. Hardtke (Ohio univ.) kindly answered my frequent questions about the NA44 programs and experiment. I made the most communication with Dr. Dennis M. Reichhold (Ohio univ.) about the analysis of the kaon interferometry.

I am very grateful to everyone who supported me, those I worked with, and those I met, at the High and Intermediate Energy Physics group and the Hadron group of Hiroshima university. Prof. Yoshio Sumi gave me helpful encouragement and support with his profound knowledge.
Prof. Toru Sugitate has continuously supported me and set forth directions for my research with his wonderful experience. Prof. Atsushi Sakaguchi helped me with his expert advice about the method of the HBT analysis. Dr. Masashi Kaneta and Dr. Hiroaki Ohnishi gave me their useful suggestions and helpful discussion. I think I am lucky to work with them.

I also thank to Prof. Takashi Ohsugi for their helpful advice and late

Prof. Osamu Miyamura for their valuable suggestions. I deeply discussed about physics and philosophy with Dr. Kensuke Homma. It is joyful and helpful that discussions with Mr. Akitomo Enokizono, Mr. Tomoaki Nakamura, Mr. Takashi Hachiya and the other colleagues in our group. I must not forget to acknowledge all of staff of Hiroshima university, especially, Ms. Hideko Masuda and Ms. Kanae Hayashi for their kind help.

I would also like to thank a lot of peoples met at the Brookhaven National Laboratory, who gave me advanced knowledge of physics experiment. Several sojourns at the BNL are joyful and memorable for my life.

I wish to thank late M.Sc. Kazuhiro Kaimi. I succeeded his analysis which greatly contributed this thesis. I would like to dedicate this thesis to him. Finally, I must thank my family and all my friends for giving me cheerful support.

Bibliography

[1] U. W. Heinz, Nucl. Phys. A **685**, 414 (2001) [arXiv:hep-ph/0009170].

[2] CERN Press Release, Feb. 10, 2001:
`http://cern.web.cern.ch/CERN/Announcements/2000/NewStateMatter/`

[3] U. W. Heinz and M. Jacob, arXiv:nucl-th/0002042.

[4] T. Matsui and H. Satz, Phys. Lett. B **178**, 416 (1986).

[5] C. Gerschel and J. Hufner, Ann. Rev. Nucl. Part. Sci. **49**, 255 (1999) [arXiv:hep-ph/9802245].

[6] M. C. Abreu *et al.* [NA50 Collaboration], Phys. Lett. B **477**, 28 (2000).

[7] R. Hanbury-Brown and R. Q. Twiss, Nature **178**, 1046 (1956).

[8] G. Goldhaber, S. Goldhaber, W. Lee, and A. Pais, Phys. Rev. **120**, 300 (1960).

[9] U. A. Wiedemann and U. W. Heinz, Phys. Rept. **319**, 145 (1999) [arXiv:nucl-th/9901094].

[10] U. W. Heinz and B. V. Jacak, Ann. Rev. Nucl. Part. Sci. **49**, 529 (1999) [arXiv:nucl-th/9902020].

[11] G. Bertsch, M. Gong and M. Tohyama, Phys. Rev. C **37**, 1896 (1988).

[12] S. Pratt, Phys. Rev. D **33**, 1314 (1986).

[13] S. Pratt, Phys. Rev. D **33**, 72 (1986).

[14] S. Pratt, T. Csoergoe and J. Zimanyi, Phys. Rev. C **42**, 2646 (1990).

[15] G. Bertsch, M. Gong, L. D. McLerran, P. V. Ruuskanen and E. Sarkkinen, Phys. Rev. D **37**, 1202 (1988).

[16] T. J. Humanic *et al.* [NA35 COLLABORATION Collaboration], Z. Phys. C **38**, 79 (1988).

[17] H. Appelshauser *et al.* [NA49 Collaboration], Eur. Phys. J. C **2**, 661 (1998) [arXiv:hep-ex/9711024].

[18] M. M. Aggarwal *et al.* [WA98 Collaboration], Eur. Phys. J. C **16**, 445 (2000) [arXiv:hep-ex/0003009].

[19] M. Gyulassy and S. S. Padula, Phys. Rev. C **41**, 21 (1990).

[20] U. W. Heinz, B. Tomasik, U. A. Wiedemann and Y. F. Wu, Heavy Ion Phys. **4**, 249 (1996) [arXiv:nucl-th/9606041].

[21] S. Bernard, D. H. Rischke, J. A. Maruhn and W. Greiner, Nucl. Phys. A **625**, 473 (1997) [arXiv:nucl-th/9703017].

[22] S. Soff, S. A. Bass, D. H. Hardtke and S. Y. Panitkin, arXiv:nucl-th/0109055.

[23] R. Billinge *et al.*, CERN-90-01.

[24] Y. Miake *et al.*, CERN/SPSC/88-37.

[25] T. J. Humanic *et al.* [NA35 Collaboration], Z. Phys. C **38**, 79 (1988).

[26] N. Maeda, S. Esumi, S. Nishimura, A. Sakaguchi, T. Sugitate, Y. Sumi and F. Nishiyama, Nucl. Instrum. Meth. A **346**, 132 (1994).

[27] N. Maeda Ph.D thesis of Hiroshima univ. (1996).

[28] P. Giubellino, et al. Nucl. Instrum. Meth. A **288**, 68 (1990).

[29] T. Kobayashi and T. Sugitate, Nucl. Instrum. Meth. A **287**, 389 (1990).

[30] C. W. Fabjan *et al.*, Nucl. Instrum. Meth. A **367**, 240 (1995).

[31] M. Spegel [NA44 Collaboration], Nucl. Instrum. Meth. A **433**, 366 (1999).

[32] D. E. Fields *et al.*, Nucl. Instrum. Meth. A **349**, 431 (1994).

[33] I. G. Bearden *et al.* [NA44 Collaboration], Nucl. Phys. A **661**, 55 (1999).

[34] D. C. Carey, K. L. Brown and F. C. Iselin, SLAC-0246

[35] I. G. Bearden *et al.* [NA44 Collaboration], Nucl. Phys. A **661**, 435 (1999).

[36] W. A. Zajc *et al.*, Phys. Rev. C **29**, 2173 (1984).

[37] T. Peitzmann, Z. Phys. C **59**, 127 (1993).

[38] I. G. Bearden *et al.*, Phys. Rev. C **58**, 1656 (1998).

[39] H. Boggild *et al.*, Phys. Lett. B **302**, 510 (1993) [Erratum-ibid. B **306**, 418 (1993)].

[40] H. Boggild *et al.* [NA44 Collaboration], Phys. Lett. B **349**, 386 (1995).

[41] H. Beker *et al.*, Phys. Rev. Lett. **74**, 3340 (1995).

[42] H. Beker *et al.*, Z. Phys. C **64**, 209 (1994).

[43] I. G. Bearden *et al.* [the NA44 Collaboration], Phys. Rev. Lett. **87**, 112301 (2001) [arXiv:nucl-ex/0107005].

[44] U. A. Wiedemann, P. Scotto and U. W. Heinz, Phys. Rev. C **53**, 918 (1996) [arXiv:nucl-th/9508040].

[45] S. V. Akkelin and Y. M. Sinyukov, Phys. Lett. B **356**, 525 (1995).

[46] A. N. Makhlin and Y. M. Sinyukov, Z. Phys. C **39**, 69 (1988).

[47] K. Kaimi *et al.*, Z. Phys. C **75**, 619 (1997).

[48] I. G. Bearden *et al.*, Eur. Phys. J. C **18**, 317 (2000).